Ru and RuO_2 as bottom electrodes for HZO based FTJ's

June 2023
EIT - LTH

Emil Gränsmark
em7234gr-s@student.lu.se
Supervisor: Mattias Borg
Co-Supervisor: Robin Athle
Examinator: Erik Lind

Lunds Universitet
Lunds Tekniska Högskola

1 Abstract

A ferroelectric material that shows great potential for FTJ's in the modern day is hafnium-zirconium-oxide (HZO) as it is compatible with Si, well established in the semiconductor industry, as well as being able to retain ferroelectricity in ultrathin films. Issues however lie in the fact that for FTJ's, HZO lacks sufficient endurance and has a long wake-up[1]. However, these detrimental effects have the potential to be reduced by using the correct electrodes. In this thesis, the established bottom electrode TiN is compared to the novel bottom electrodes Ru and RuO_2 to see if these new electrodes have the possibility of enhancing both the endurance and the polarisation at thinner HZO thicknesses.

Ru and RuO_2 had not been sputtered in this lab before, so the results were not optimised, as the resistivity for the RuO_2 was around 4 times as large as reported values.

The 10 nm HZO thick samples were annealed at 500°C, whilst the 6 and 4.5 nm samples were annealed at both 500°C and 550°C. PUND measurements were done and results show that both Ru and RuO_2 (20% O) have a larger polarisation than TiN at 10 nm, although RuO_2 breaks down early. Going down in thickness to 6 nm, Ru keeps a healthy $2P_r$ of $33\mu C/cm^2$ at 550°C compared to $28\mu C/cm^2$ at 500°C, showing that a temperature increase helps with the polarisation.

At 4.5 nm there were no ferroelectricity for any bottom electrode at 500°C and only weak ferroelectricity at 550°C. An exception for this is RuO_2 (20% O), which shows a $2P_r$ of $20\mu C/cm^2$ even though it breaks down at around 10^5 cycles.

From the results of these measurements, it seems like whilst the $Ru(O_2)$ bottom electrodes outperform TiN when it comes to an increased polarisation, they fail to perform their primary function of increasing the endurance.

2 Popular science summary

Vår hjärna löser beräkningar som tar oss genom livet otroligt energieffektivt; den kör hela dagen runt på ungefär 12 watt. Jämför man med en vanlig dator som kräver ungefär 175 watt så är det inte ens nära[2].
Att uppnå hjärnans energieffektivitet är ett ambitiöst mål för dagens elektronik. Tricket ligger i att efterlikna hjärnans struktur och uppbyggnad med elektroniken. Detta forskningsområde kallas neuromorphic electronics, och är ett hett område just nu.
Hjärnan är ett flexibelt organ, med möjligheter att anpassa sig till nya situationer. Synapserna, som binder ihop alla hjärnans neuron till ett stort nätverk, är nyckelen till detta. De kan, beroende på storleken och frekvensen av signaler de tar emot, skapa svagare eller starkare förbindelser mellan neuronen. Att bygga något som följer samma princip hade varit ett stort steg i att konstruera en artificiell hjärna.
En komponent som visat potential till att lösa denna uppgift är en FTJ; en Ferroelectric Tunnel Junction. Det är ett relativt simpelt koncept som efterliknar en smörgås, man har ett tunt lager ferroelektriskt material(pålägget) mellan två elektroder(brödet). Målet är att kunna styra hur många elektroner som kan tunnla igenom lagret och bidra till strömmen som går igenom FTJ'n, och detta kan göras tack vare det ferroelektriska materialet. Ett ferroelektriskt material kan ändra sin polarisation under ett elektriskt fält, och behåller en del av polarisationen när fältet slås av. Detta är en värdefull egenskap. Polarisationen i den tunna filmen kommer då ses som ytladdningar som måste kompenseras av laddningar i elektroderna. Har man en asymmetri mellan elektroderna (olika laddningsbärardensitet eller arbetsfunktion) så kommer ytladdningarna kompenseras olika. Då skapas två olika barriärer för elektronerna att tunnla igenom beroende på vilket håll polarisationen pekar åt. Den ena barriären är hög, den andra är låg.
Men det behöver inte nödvändigtvist vara så binärt, utan man kan ha en stor mängd olika barriärshöjder beroende på styrkan och frekvensen av det elektriska fältet man lägger på. Det är denna egenskap som tillåter FTJ'n att bete sig som en synaps i din hjärna.
Svårigheter med att konstruera FTJ'er idag är att de ferroelektriska lagren har låg polarisation vid tunna lager, och att de har låg uthållighet och lätt går sönder efter att ha cyklats mycket. Materialet hafnium-zirkonum-oxid (HZO) visar mest potential just nu, men har låg uthållighet på grund av defekter. En nytt material som föreslagits som elektrod i en HZO-baserad FTJ är rutenium (Ru) och ruteniumoxid (RuO_2).Dessa material kan i teorin motverka dessa defekter och förbättra uthålligheten, vilket hade tillåtit HZO-baserade FTJ'er att komma ett steg närmre en spännande framtid.

3 Acknowledgements

I'd like to thank my supervisors Mattias and Robin for providing me with such a great opportunity to work with research and just generally helping me out in my time of need. Big ups to Robin and the LNL gang for teaching me the tools and the measuring. I'd also like to thank Duc, Karthik, Hannes, André, and all the other lovely people at the EIT department for being helpful and good company. Last but not least, I'd like to thank my family and friends, especially Rinko, Konke, Joel, and Wille for helping me recharge my mental batteries every day.

"That has to be the worst sample I've ever seen"
- Robin Athle (paraphrased)

4 Abbreviations and acronyms

FeFET - Ferroelectric Field Effect Transistor
FeRAM - Ferroelectric Random Access Memory
FTJ - Ferroelectric Tunnel Junction
CMOS - Complementary Metal-Oxide-Semiconductor
HZO - Hafnium-zirconium-oxide
E$_c$ - Coercive field
P$_r$ - Remnant polarisation
P$_s$ - Saturated polarisation
FE - Ferroelectric layer
TER - Tunneling electroresistance
BEOL - Back-end-of-line
LNL - Lund Nanolab
CTE - Thermal expansion coefficient
MIM - Metal-Insulator-Metal
ALD - Atomic layer deposition
PVD - Physical vapour deposition
DC - Direct current
RF - Radio frequency
CVD - Chemical vapour deposition
RTA - Rapid thermal annealing
sccm - Standard cubic centimeters per minute
TEMA - tetrakis(ethylmethylamino)
rpm - Revolutions per minute
PUND - Positive Up Negative Down
IV - Current vs voltage
PE - Polarisation vs electric field
BE - Bottom electrode
TE - Top electrode
2P$_r$ - +P$_r$ - -P$_r$

List of Figures

List of Tables

Contents

5 Introduction

Ferroelectricity is an interesting concept first discovered in 1921 by J.Vasalek when rochelle salt showed an electric hysteresis loop, revealing a permanent polarisation in the absence of an electric field[3]. Many other materials since then have shown ferroelectric properties, such as Lead titanate (PbTiO3), and Lead zirconate titanate (PZT). Ferroelectricity has paved the way for novel devices such as FeFET's (Ferroelectric Field Effect Transistor), FeRAM's (Ferroelectric Random Access Memory), and FTJ's (Ferroelectric Tunnel Junction). Ferroelectric materials widely studied for these devices are perovskites like PZT, showing retention times up to 45 years and endurances up to 10^{15} cycles[4]. These materials also have their issues when it comes to certain devices such as the FTJ, such as a decrease in ferroelectricity when scaling down and poor integration with CMOS. An alternative needed to be found, and in 2011 hafnium-dioxide (HfO_2) was discovered to have a ferroelectric phase[5]. It could be scaled down to a few nm and retain its ferroelectricity, allowing it to function as a tunnel barrier with the two polarisation states acting as the ON and OFF state. The material was already established in the semiconductor industry as gate oxides and dielectrics and was thus an easy choice. Doping the HfO_2 with zirconium (Zr) to make hafnium-zirconium-oxide (HZO) shows even larger polarisation values than just HfO_2 and has been a promising candidate as the ferroelectric film used in FTJ's[6]. Issues with hafnium-based ferroelectrics have been a smaller endurance of $<10^{10}$ cycles but that The electrodes utilised in FTJ's play an important part in achieving and maintaining ferroelectricity in the HZO film. Choosing an electrode that facilitates enough tensile stress to encourage growth of the ferroelectric phase[6] in the HZO as well as minimising any defect generation that might degrade the quality of the film is crucial[7].
This thesis will test the novel Ru and RuO_2 metal oxides as bottom electrodes for FTJ's with thin HZO films and compare both the polarisation and endurance with a standard bottom electrode, TiN. The hypothesis is that the $Ru(O_2)$ electrodes will improve the endurance and polarisation by providing a lower thermal expansion coefficient, higher work function difference, and reducing the amount of oxygen-vacancies in the HZO film.

6 Background

6.1 Polarisation

A crystalline material consists of tiny building blocks called unit cells. This unit cell is the smallest repeating component of the crystal and contains a number of atoms in a three dimensional ordered fashion[8].

An asymmetric molecule such as water has a dipole moment with the separation of the hydrogen and oxygen atoms (a pair of opposite charges separated by a certain distance is called a dipole, and a dipole moment is the product of the charge and the distance). A unit cell can also display this behaviour.

Insulating materials that can be polarised by applying an electric field are called dielectrics. There are certain sub classes of dielectrics, including piezoelectrics, pyroelectrics, and ferroelectrics. Refer to figure 1.

These require a non-centrosymmetric crystal class, meaning that the unit cell is not symmetric around its centre. Piezoelectrics display polarisation when mechanical stress is applied, as the force will shift the dipoles in the material, separating the positive charges from the negative charges.

Pyroelectrics are a subgroup of piezoelectrics which can have their spontaneous polarisation changed with temperature. A spontaneous polarisation is when the material is polarised without any external factors in play.

If the spontaneous polarisation of a pyroelectric is able to switch because of an external electric field, it is known as a ferroelectric. This subgroup is also known as a nonlinear dielectric, as opposed to a linear dielectric where the polarisation is linearly related to the electric field. A more in depth explanation of this nonlinearity will be discussed later in chapter 6.2.

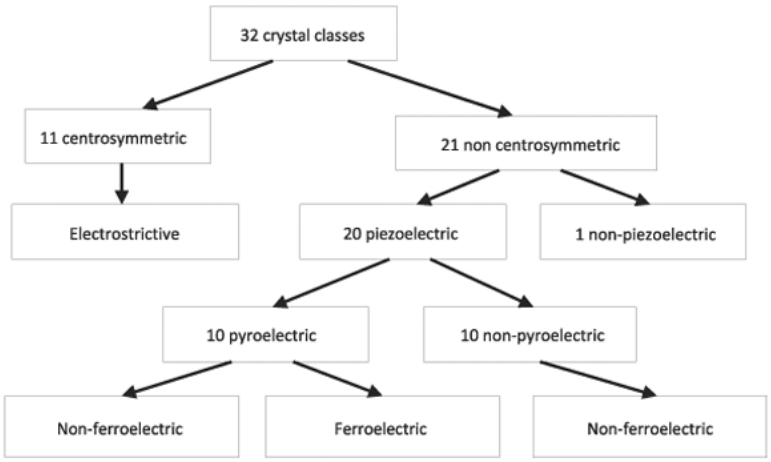

Figure 1: Classes and subclasses of the 32 crystal classes. Taken from [9].

6.2 Ferroelectricity

A ferroelectric material has two or more stable states; it can switch between these given a large enough electric field. The switching mechanism can be simply explained by taking a hypothetical, one-dimensional crystal with atoms of opposing charge as shown in fig.2.

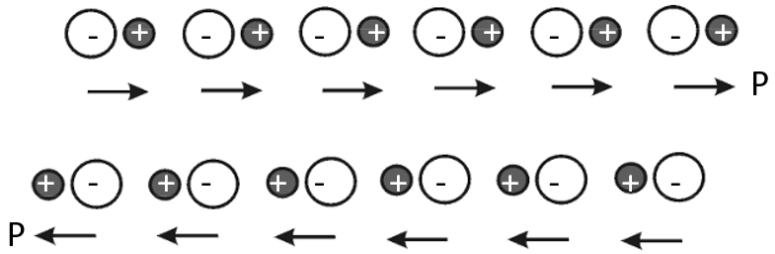

Figure 2: One-dimensional crystal showing the two metastable states of a ferroelectric material. Taken from [10].

If the physical positions of the atoms in the unit cell are in a certain positions, all the dipoles created by this structure will create a polarisation pointing in the one direction. This is a stable state. To switch it to the second stable state, one would need to apply enough energy to shift the positions of the atoms in the unit cell to reverse the polarisation. The states in fig.2 are identical in terms of energy; they only differ in the polarisation direction, one being negative and

the other being positive in relation to ground[10].
Because of the fact that an electrical field is needed to move the atoms in the unit cell, there is an energy barrier between the two states. Increasing the electric field means moving the atoms closer, lowering the barrier, until the atoms are in the opposite position as before. The process can be seen in fig.3.

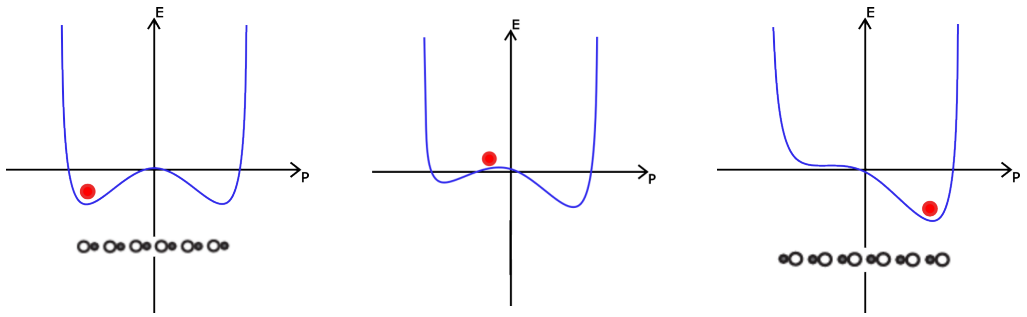

(a) Negative polarisation, no electric field applied.

(b) Energy barrier between polarisation states lowers with electric field.

(c) Atoms have changed place and the polarisation is positive.

Figure 3: Polarisation switching through energy states. One-dimensional crystal structures that correspond to the current polarisation states are shown in the respective subfigure.

Even though each unit cell in a ferroelectric material exists only in either one of the polarised states, the polarisation in the whole film is far from uniform. Groups of dipoles pointing in the same direction are called domains, and the directions of the domains are what cause the polarisation of the film. Domains can be ordered along different polar axes or along the same axis but with opposite polarity[11]. A polar axis is a direction in a crystal that is not transformed in the opposite direction when any symmetry operation is performed on the crystal[12]. The existence of domains can be explained by thermal and electrical history of the film, non-uniform strain, and defects[10].

Depending on the domains alignment to the electric field, and if the domains have difficulty switching because of being pinned, they will switch at different voltages, i.e they will have different coercive fields E_c[13]. In a perfect world, all domains would have the same coercive field. But this is not a perfect world. This means that the switching of polarisation in the ferroelectric film is never instantaneous, but gradual. The switching can be improved by cycling the film, gradually de-pinning domains. This effect is called wake-up.

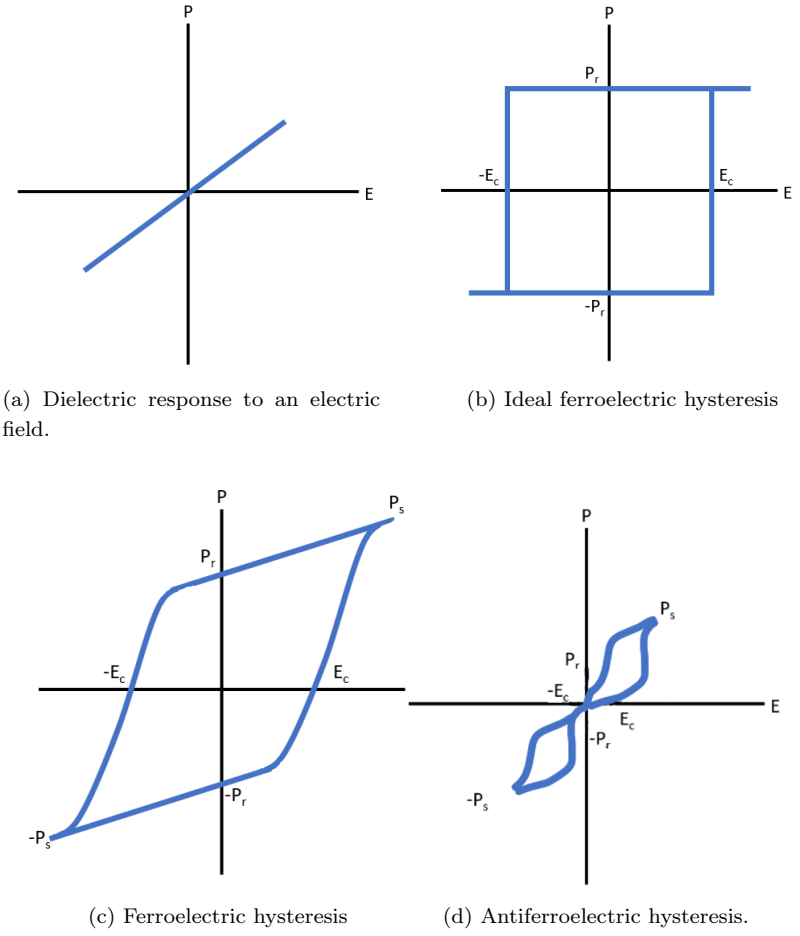

(a) Dielectric response to an electric field.

(b) Ideal ferroelectric hysteresis

(c) Ferroelectric hysteresis

(d) Antiferroelectric hysteresis.

Figure 4: Different hysteresis curves depending on the type of dielectric.

This ties in to the hysteresis and ferroelectrics. In fig.4a, the common dielectric response to an electric field can be seen. The polarisation is calculated using eq.1

$$P = \frac{Q}{A} \tag{1}$$

where P is the polarisation in $\mu C/cm^2$, Q is the charge and A is the area. The polarisation will increase as the charge increases, as can be seen in eq.2.

$$Q = CV \tag{2}$$

Where Q is the built up charge, V is the voltage, and C is the capacitance. Thus, the polarisation increases with the voltage from the electric field.
In fig.4b, the ideal hysteresis of a ferroelectric material can be seen. This is the ideal behaviour of a ferroelectric as the all the domains have the same alignment and meaning they switch at the same coercive field, and the remnant polarisation P_r is equal to the saturated polarisation P_s,

which occurs when all the domains that are available for alignment have been aligned.
Moving towards the unfortunate reality of the ferroelectric hysteresis, we can see in fig.4c that the switching is not at all instant, neither is the remnant polarisation equal to the saturated polarisation.
A special property that some materials possess is antiferroelectricity, and its hysteresis can be seen in fig.4d. These materials have their dipoles align opposite each other at no electric field, cancelling each other out. One cause for their unique double hysteresis loops are the field-induced reversible phase transitions between antiferroelectric and ferroelectric phases[14]. This feature allows antiferroelectrics to be used in applications such as high-energy storage[15], because these applications require the highest possible saturated polarisation as well as the lowest remnant polarisation[16].

6.3 FTJ's

The waveform of an electron can extend beyond a potential barrier, making the probability of the electron to appear on the other side finite. This phenomenon is known as tunneling. Electrons tunneling through a potential barrier is a common concept in quantum physics, and the probability of tunneling depends exponentially on the height and width of the barrier. The probability of transmission follows depends exponentially on both barrier thickness and barrier height[17].

This phenomenon gives rise to a device known as a tunnel junction, where a insulator tunnel barrier is sandwiched between two, usually metal, electrodes.
The idea of an FTJ came from Esaki et al in 1971[18].
An FTJ works by having a ferroelectric material (FE) between two electrodes (M1 and M2). Refer to the bottom part of fig.5. As the FE is polarised, bulk charges cancel each other out but leaves bound surface charges at the FE/M interface that will attract or repel electrons depending on which way the polarisation is pointing. Some of the charges from the electrodes will cancel out, or screen, the surface charges. If the surface charges in the FE are not completely screened, there will be a depolarisation field in the FE[19]. This depolarisation field opposes the internal polarisation field in the FE[17]. The depolarisation field can also be caused by passive interfacial layers, usually referred to as dead layers. By having electrodes with different screening lengths (the distance from the interface to the point in the electrode when the electron concentration has returned to equilibrium), there will be an asymmetric potential profile[19].
In fig.5, we have two cases. The left is when the polarisation points to the right, so the positive surface charges cause an accumulation of electrons on the electrode side of the interface. Because M2 has a larger screening length δ_2, the potential drop will be larger than if the polarisation were to point towards M1 that has a smaller screening length δ_1.
The differences in potential drop over the interfaces causes different average barrier heights (ϕ_- and ϕ_+, and the transmission probability is exponentially proportional with barrier height. This is what causes tunnel electroresistance (TER)[20].
The asymmetry at the interfaces need not only be because of different electrode materials, but can be because of dead layers with no charges, different interface terminations, and ionic screening[17].

Whilst the usual electrodes would be metal, metal oxides[21] and semiconductor[22; 23; 24] electrodes have been thoroughly researched. While metal provides screening as shown in fig.5, semiconductor electrodes with their lower carrier density will provide fewer charges to screen. The depletion field on the semiconductor side of the interface will then increase the Schottky barrier thickness, causing a larger TER[24].

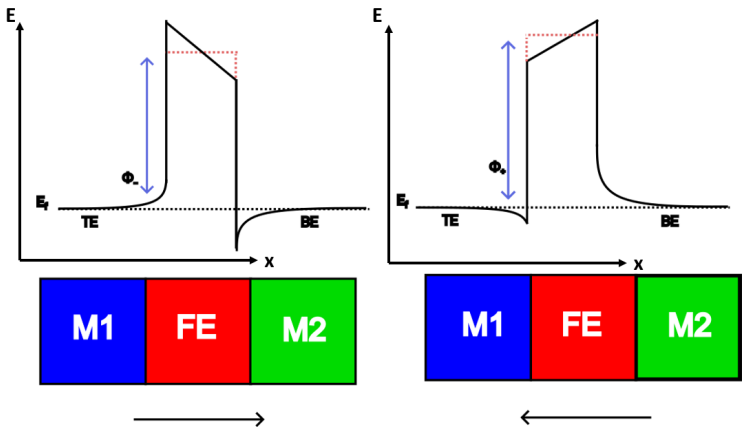

Figure 5: Potential barrier energy at opposing polarisations plotted vs position of the MIM. Red dotted line is the average barrier height. Black dotted line is the Fermi level.

There are four different ways for electrons to be transported across the FE barrier.
The first, and most intuitive, is direct tunneling. It is the same as the tunneling mentioned previously, and it is the main contributor for current at thin/low barriers (<4 nm) and at low electric fields.
Thermionic injection, when electrons are given sufficient kinetic energy from a temperature increase to overcome the barrier. This is dominant at low voltages but thicker films (>5 nm).
Fowler-Nordheim tunneling (FN tunneling) is when an electric field is applied so that a potential barrier is low enough for the electrons to tunnel through. This transport mechanism dominates at high electric fields[17]. Refer to fig.6.
There will always be defects introduced into the thin FE film during deposition, and these can act as available lower-potential states for electrons to tunnel to. They can then tunnel through to the other side of the barrier very easily since the barrier, thus the energy required, is reduced[25].

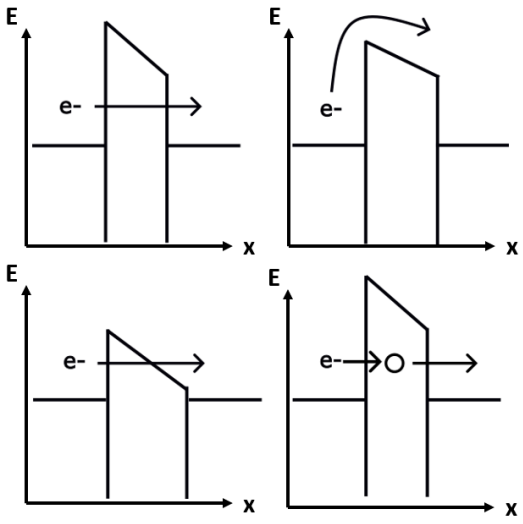

Figure 6: Different electron transports through the potential barrier. Plots show energy versus position in the MIM. Top left: Direct tunneling, Top right: Thermionic injection, Bottom left: FN tunneling, Bottom right: Trap assisted tunneling

Having the two polarisation states leads to the FTJ being able to act like a binary device. It either has low resistance (ON state) or it has high resistance (OFF state). This can be very useful in some cases, but in other cases like neuromorphic electronics, it can be beneficial to have more granularity.
A memristor, the so called fourth missing passive circuit element is a device that relates flux linkage with charge. A device shows memristic behaviour if its resistance can be continuously tuned[26].
This concept can be used with FTJ's. Domains do not necessarily switch at the same voltage[13], but the percentage of aligned domains can be controlled using voltage pulses. The FTJ's resistance is dependent on its polarisation, which in turn is dependent on the aligned domain percentage. This naturally leads to the conclusion that an FTJ can also be used as a memristor[27].

The uses of an FTJ are many. It can be used for neuromorphics computing, where each FTJ would act as a synapse. It would mimic the spike time dependent plasticity of the synapse by gradually increasing the FTJ's resistance every time it is subjected to a voltage pulse. This principle can be used to create artificial neural networks, utilising the same process to create low-power tunable analogue tunnel current that can perform vector-matrix multiplication when combined with an analogue voltage input[28]. Non-volatile memories are also an interesting potential application, using the remnant polarisation as information storage[20; 23].

6.3.1 HZO

Some ferroelectric materials that are potential candidates for electronic devices are PZT and $BaTiO_3$. Unfortunately they often run into problems such as a bad Si-interface because of an SiO_2 formation, or a low bandgap and poor scalability which counts them out for tunneling devices or memory applications[14; 29].

Luckily, in the year of 2011, Böscke et al made the discovery that Si doped HfO_2 could show ferroelectricity if doped correctly and annealed under mechanical stress[5]. An advantage that HfO_2 has is that it is thermodynamically stable on Si, the most important material in modern electronics, as well as being an already established part of semiconductor fabrication[30]. This opens up the potential for it to be used in all kinds of devices that require a Si-FE interface, such as an FTJ. Whilst other FE oxide films such as $SrTiO_2$ also show compatability on Si, HfO_2's high valence band offset compared to Si makes it more attractive for low leakage devices such as memory applications, and its ability to show ferroelectricity at tunneling-level thicknesses makes them attractive for FTJ's[31].

Another option to HfO_2 is hafnium-zirconium-oxide (HZO). Its ferroelectric property was first reported in 2012[6]. Its ferroelectricity is said to originate from the non-centrosymmetric orthorhombic phase $Pca2_1$, and shows the greatest ferroelectric response at 50 mol % Zr, but the composition can be varied to achieve antiferroelectricity which can be used for other applications[14]. Because both HfO_2 and Zr_2 are already established in fabrication and thus used in electronics and since the atoms are of similar size, the HZO alloy is a natural evolution.

HZO shows some strict requirements to obtain the orthorhombic crystal phase $Pca2_1$. The first is the correct annealing temperature, where it has an advantage over conventional FE materials. Conventional FE materials need to be annealed at high temperatures to achieve the uniform crystal phases needed for ferroelectricity. This requirement can be detrimental when it comes to integrating these devices in the back-end-of-line (BEOL)[32; 33].
HZO shows a lower annealing temperature (400-500°C) needed to achieve the orthorhombic crystal phase giving it ferroelectricity, making it suitable for BEOL[33; 14].
The other requirement is that HZO needs to be under mechanical stress during annealing, as the origin of its ferroelectricity comes from the transformation from the non-ferroelectric tetragonal phase to the ferroelectric orthorhombic phase through in-plane tensile strain[34]. This phase transition has been reported to be a thermally activated process, making its ferroelectricity increase with temperature [35; 36]. The way to achieve this stress during annealing is by depositing a "capping" layer before annealing. This is usually the top electrode, but another layer (called a crystallisation electrode) can be used during deposition only to help with crystallisation and then be removed in favour of the top electrode[37]. There is a certain sweet spot for ferroelectricity in HZO, with the film thickness being between 5 and 20 nm[38]. Scaling further leads to a reduced orthorhombic phase which in turn leads to a lower polarisation. The cause of the reduced orthorhombic phase has been reported to be the dead layer[39]. Apart from detrimental effects on

ferroelectricity such as improper mechanical stress, other factors also affect the properties of the HZO film's performance in an FTJ. The main one being interfacial bound charges, A large source of these defects are oxygen vacancies at the electrode-FE interface, which can occur during the deposition and the annealing step[7]. The accumulation of these oxygen vacancies are a cause for poor endurance and long wake-up because of them pinning domains, causing them to have a harder time switching[7]. They are also a cause for coercive field asymmetry[40; 41]. It has been reported that the coercive field also increases when the FE thickness decreases[42].

6.3.2 Electrodes

The electrodes are as mentioned before a crucial part of not only achieving a good TER but also making sure that the HZO film is properly ferroelectric. An important role for all electrodes is having a low resistivity, as the electrodes need to be conductive and allow as much as possible of the applied voltage to fall over the oxide.
The electrodes used in this thesis are tungsten (W) as a top electrode, and titanium-nitride (TiN), ruthenium (Ru), and ruthenium-oxide (RuO_2) as bottom electrodes.
As W and TiN are mature processes and heavily studied in LNL, they are used as reference samples, and only the bottom electrode is switched out for Ru and RuO_2.
When it comes to providing proper tensile strain to help HZO crystallise in the orthorhombic phase, the thermal expansion coefficient (CTE) plays a part. This is because a decreasing CTE tends to change the in-plane strain from compressive to tensile[40; 43].
W has a CTE of $4.5 \cdot 10^{-6}$ K^{-1}, whilst TiN, Ru, and RuO_2 have 9.4, 6.4, and $5.2 \cdot 10^{-6}$ K^{-1} respectively[7]. That makes W an excellent choice to contribute plenty of tensile stress.
Together with the screening length difference[17], the work function of the electrode also plays a role. A larger difference in work function between the electrodes gives us a larger TER; an important parameter to increase[37]. It also shifts the coercive field as it creates a large built-in field that opposes the depolarisation field. And as the depletion field increases with both decreasing thickness and a thicker dead layer, a large work function difference certainly helps[44].
The work functions of W, TiN, Ru, and RuO_2 are 4.5 eV[45], 4.65 eV[46], 4.71 eV[45] 5.1 eV[47]. This makes Ru and RuO_2 attractive options.

Another important aspect of the electrodes is if they have a good interface with the FE. During the annealing step, the electrodes will undergo an oxidation reaction with the HZO, and depending on the degree of oxidation you will get different amounts of dead layer and oxygen vacancy defect generation[48]. Since it has been reported that oxygen vacancies are detrimental for coercive field asymmetry and endurance[41; 7], electrodes that reduce this effect are preferred. Whilst TiN is an attractive material for an electrode in a device with HZO because of its compatability with Si, its low cost, and its ability to act as a barrier against incorporation of hydrogen[14], it can scavenge oxygen from the HZO film during the annealing step. The diffusion of oxygen into the TiN layer would then be a source of oxygen vacancies[40] and the creation of the non-ferroelectric dead layer[48]. In contrast to TiN, RuO_2 could instead act as a oxygen vacancy sink, providing oxygen atoms to the HZO and thus reducing the amount of vacancies[7].

Using Ru and RuO_2 as a metal oxide electrode for MIM's has been studied because of its potential properties causing fewer defects in the HZO layer and of acting as an oxygen sink for the ferroelectric layer/electrode interface[7; 49; 50] as well as reducing the dead layer effect thanks to a partial polarisation of the electrode itself[51].
Fabricating the material has been done with both ALD[7; 52] and by sputtering[51; 53; 54], but in the case of this report, sputtering was used.
Reported resistivities of RuO_2 and Ru are $<$100 $\mu\Omega cm$ and 16-30 $\mu\Omega$cm respectively.[51; 53; 54].

6.4 Processing

6.4.1 Sputtering

Sputtering is a type of physical vapour deposition (PVD) that allows thin films to be deposited on a substrate. The substrate is placed in a vacuum chamber together with a target, which is the material that is to be deposited. The vacuum is to avoid any stray particles to contaminate the surface[55] of the substrate.
An inert gas, often Ar, flows into the chamber to generate a plasma. This is done by applying a high voltage behind the target, and applying ground behind the substrate, see fig.7. This causes the electrons from the inert gas to accelerate away from the target, and during this acceleration they may collide with an atom in the gas. This collision knocks off an electron from the atom, creating a positively charges ion which then accelerates towards the target. These high-velocity ions strike the target with enough force that the target material is "sputtered", and the sputtered material has enough energy to reach the substrate, eventually creating a film[55].

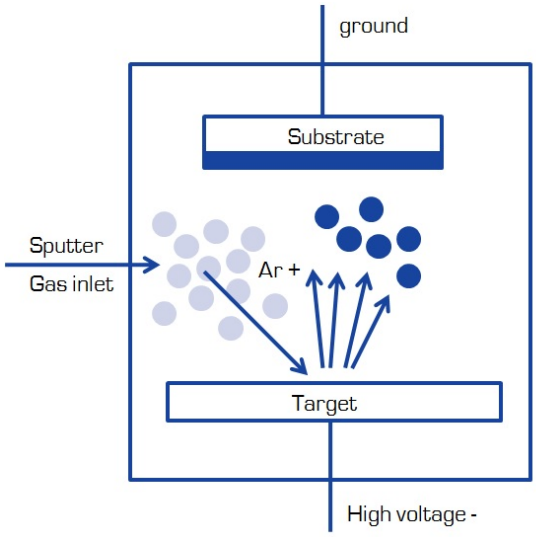

Figure 7: Diagram of a sputtering chamber. Taken from [56].

Other gases can be allowed into the chamber to react with the sputtered target to instead

deposit a new film, such as having O_2 react with Al to deposit Al_2O_2 on a substrate[55].
Magnetron sputtering is common since ions can be controlled by a magnetic field. It uses the field to increase deposition rates, increase plasma density, and decrease potential damage to the substrate and film[55].
Both DC and RF power sources can be used when sputtering. When sputtering a dielectric material it can be beneficial to use an RF source to avoid a charge build up[57].

6.4.2 ALD

Atomic layer deposition (ALD) is a type of chemical vapour deposition (CVD) which allows thin uniform films to be deposited in a controlled manner.
A substrate is placed in a vacuum chamber, and two or more precursor gases are introduced to react with each other on the sample, creating the film. The precursor gas pulses are alternating and are separated by a purge phase, where an inert gas clears the chamber of the previous precursor gas to avoid any gas phase reactions with the next precursor gas. Refer to fig.8.

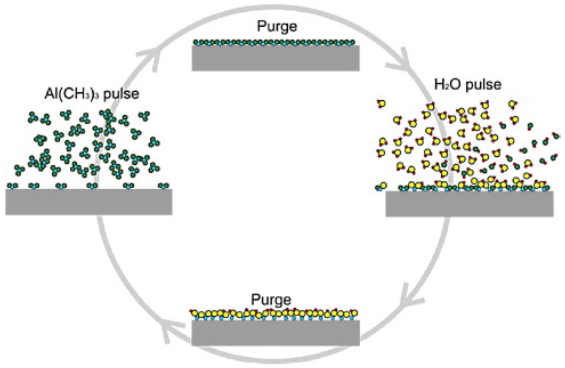

Figure 8: ALD pulse/purge cycle with an example reaction. Taken from [58].

The ALD process is limited by surface chemistry, as one of the gases will only contribute to forming a layer of the film as long as there are reactive sites available. Ideally, this would lead to a perfectly uniform and conforming atomic layers, although typical growth rates are less than half a monolayer per cycle[58].
There are several parameters that control the ALD process. The pulse times for the precursor gases have to be long enough to react with the entire surface, and the purge times have to be long enough to clear the chamber fully. Because of time and money constraints of modern industry, these pulse and purge times should be kept as short as possible[59].
There is also a temperature window of ideal ALD processing. Too low temperatures lead to slower reactions or precursor condensation, and too high temperatures lead to precursor desorption[59].

6.4.3 RTA

RTA, or Rapid Thermal Annealing is a process that rapidly heats up a sample with the intention to change electrical, material, or interfacial properties. In the case of HZO, the annealing plays a part in crystallising the film to achieve a large amount of the orthorhombic phase $Pca2_1$[36].

6.4.4 Spin coating

Spin coating is an easy way to apply a thin and uniform layer of resist for photolithography on a flat sample. The process is initiated by a soft bake step, where the sample is heated to enhance adhesion. The sample is then placed on a chuck and is held in place using a vacuum, and then a few drops of resist is deposited on the sample. Afterwards the sample is spun around quickly, forcing the resist outwards so it covers the whole sample. Resist thickness can be decided by varying the spinning speed, or by the surface tension and viscosity of the resist. After the spinning, the sample is once again heated in a post-exposure baking step to prevent film flaking.

6.4.5 Mask aligning and exposure

After depositing a thin film of photoresist on a sample, the next step in a process is to develop the desired pattern for further processing. By placing the sample in a mask aligner, a mask containing the pattern is placed over the sample. The mask is adjustable by the user, to ensure proper alignment and placement of the pattern on the sample. Afterwards, the sample undergoes exposure, in this case by a UV light source. The exposure strength is decided by the exposure time and the wavelength of the light. Depending on the type of resist, the exposing light will either break the polymer bonds (positive resist) and make it soluble to the developer or polymerise it (negative resist) and make it insoluble to the developer.

6.4.6 Plasma ashing

Used to clean off any residue resist on the sample. A plasma is generated by exposing a reactive species, oxygen in our case, to a vacuum. The oxygen ions react with the resist which is then removed. A Faraday cage can be placed over the samples to reduce the potential damage the samples can sustain from the plasma.

6.4.7 Lift off

After having a layer (of metal, for example) deposited on the whole sample, the parts covering some of the intentionally left over resist can be removed by "lifting off" the resist, bringing the deposited layer with it. This requires the resist to be isotropically etched so that the developer can reach the resist.

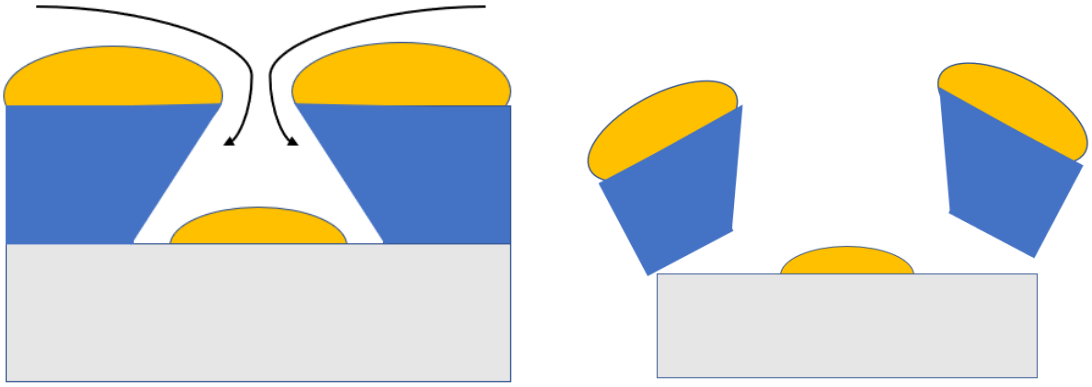

(a) Isotropic etching of the resist allows the developer to reach the resist.

(b) The metal deposited on the resist is lifted off, leaving only the metal in the desired position.

Figure 9: Lift off process.

6.4.8 Sample fabrication process

Processing the FTJ samples followed a step-by-step recipe.
Initially, the bottom electrode (TiN, Ru, RuO_2) was sputtered on a 2-inch Si wafer using an AJA Orion 5 sputterer. The TiN sputtering conditions were 150 W RF, 9 Ar sccm, 2.6 mTorr, 10 nm. The sputtering conditions of Ru/RuO_2 were 16 Ar sccm and 0, 1.78, 4, 6.86, and 16 O_2 sccm with a pressure of 4.6, 4.7, 4.9, 5.6, and 6.8 mTorr respectively, using 75 W for the first four samples and 100 W for the fifth sample. Deposition time was 600 s, following a 5 minute pre clean using only Ar. The whole process was at room temperature.

HZO of desired thickness was then deposited on the bottom electrode using a Picosun Sunale R-100 ALD. ALD deposition conditions were 200°C chamber temperature and 80°C source temperatures. Precursor sources were tetrakis(dimethylamino)zirconium/hafnium (TDMAZr/TDMAHf) using H_2O as the purge source. A layer of MaN-440 resist was spin coated on the samples following a 10 minute 110°C hotplate baking. Spin coating recipe was 6000 rpm for 45 seconds with no acceleration step. After the spin coating the samples were once again baked at 95°C for 3 minutes.
The samples were then aligned to a mask and they were exposed to 365 nm for 75 seconds.
Following the exposure was development in MaD-532/s for 105 seconds followed by H_2O for 60 seconds.
Afterwards the samples were put in a plasma asher with a Faraday cage for 30 seconds to remove the residue resist.
The top electrode W was sputtered on all the samples using 100 W DC, 9 Ar sccm, 50 nm.
The top electrode was lifted off using acetone to reveal the final device structure. The circular devices measured on have a radius of 25 μm.
The samples were annealed using a RTP-1200-100 at 500°C and 550°C for 30 s to test the temperature dependency of the FTJ.

6.5 Characterisation

The samples were analysed using tools and methods mentioned below to find their material and electrical characteristics.

6.5.1 Profilometer

A profilometer is a tool that measures surface uniformity. There are different ways for a profilometer to achieve this, but the one used here is the contact profilometer. They utilise a stylus that is dragged across the surface, and the vertical differences it undergoes as it drags across the highs and lows of the sample surface are electrically measured.
For the thickness measuring, a small piece of tape was applied to the samples during sputtering to make thickness measurements easier by providing a "step", where the deposited film would meet the clean Si. Using a Bruker Dektak XT Stylus Profilometer, an approximate thickness was extracted. A non-negligible factor during this step is that the tape was not optimally applied, so there were large portions of the "step" that were too gradual to get a proper measurement. The average was taken where there was a proper, measurable step.

6.5.2 4-point resistivity measurer

A 4-point resistivity measurer can calculate the resistivity of a thin film if the thickness is known. This works by having four colinear probes that are equally spaced, forcing a current through the outer probes and measuring the voltage between the two inner probes.
To calculate the resistivity of the samples, the tool used was a 4p probe Lucas Labs Pro4-4400. Several measurements were done at different locations on the sample, and the average was taken. The tool measures the required voltage it takes to obtain a 1 mA current. With these values along with the approximated film thicknesses from table 3, we calculate the resistivities of the samples using eq. 3 as states in the table below.

$$\rho = \frac{U}{I} \cdot 4.53 \cdot W \tag{3}$$

where 4.53 is a geometric constant and W is the film thickness.

6.5.3 Device electrical characteristics analysis

The electrical measurements were done using a B1500A Semiconductor Device Parameter Analyser and a MPI Semi-auto probe station - TS2000-SE.
Different recipes were used to extract certain data and to change some electrical properties of the devices.

Break of oxide is an increasing voltage sweep with the intention of breaking the HZO oxide to gain access to the grounded bottom electrode through the top electrode as it cannot be probed otherwise. Whilst the broken oxide provides a series resistance during measuring, it is small enough to be ignored.

Wake up is applying repeated voltage pulses alternating positive and negative pulses in order to "wake up" the ferroelectric film; that is, aligning the domains to obtain quicker switching.

PUND measurements stand for Positive Up Negative Down. These are essential to obtain information related to the ferroelectric properties of the device. After one initial pulse to set the polarisation, two consecutive positive pulses (or negative, it is arbitrary) being Positive and Up are pulsed to switch the polarisation. The first pulse (Positive) should ideally completely switch the polarisation, showing a polarisation current, whilst the second pulse (Up) should not show any polarisation current at all considering the ferroelectric film should already be completely switched. There are still some current that appears during switching, them being the leakage and the capacitive currents. Any remaining polarisation current during the second pulse is caused by any dielectric polarisation and/or trapped charges[9]. Refer to fig.10 for an example of what a PUND measurement can look like post- and pre-wake up.
From the PUND measurement, the IV measurements and the PE measurements can be made. Plotting only current versus voltage will show how the current through the ferroelectric film varies with the electric field.
To obtain the classic ferroelectric hysteresis plot, the polarisation needs to be calculated using the following equation:

$$P = \frac{Q}{A} \tag{4}$$

where P is polarisation, Q is the charge, and A is the area.
The charge is calculated by integrating the current during the Positive pulse. This gives the polarisation hysteresis including the leakage and capacitive currents that can be seen during the Up pulse. This is the "real" hysteresis plot, the pure polarisation can be plotted by subtracting the current from the Up pulse before integrating it. Data was plotted in Matlab.

Using the grown Ru and the RuO_2 (20%) bottom electrodes, the FTJ devices were fully fabricated with a 10 nm HZO film and annealed at 500°C. The samples were then taken to the B1500A Semiconductor Device Parameter Analyser and the MPI Semi-auto probe station - TS2000-SE for PUND measurements.

7 Results and discussion

7.1 Samples

All samples were fabricated and characterised similarly as stated in chapter 6.4.8 and 6.5.3 but with varying bottom electrodes, FE thicknesses, and annealing temperatures. All the samples measured on can be seen in the table 1.

Table 1: Samples used for measuring. % values are percentage of oxygen in the deposition chamber during sputtering.

BE	**HZO thickness**	**Annealing temperature**
TiN	10 nm	500°C
Ru	10 nm	500°C
RuO_2 (20%)	10 nm	500°C
Ru	6 nm	500°C
Ru	6 nm	550°C
RuO_2 (20%)	6 nm	500°C
RuO_2 (20%)	6 nm	550°C
TiN	4.5 nm	500°C
TiN	4.5 nm	550°C
Ru	4.5 nm	500°C
Ru	4.5 nm	550°C
RuO_2 (10%)	4.5 nm	500°C
RuO_2 (10%)	4.5 nm	550°C
RuO_2 (20%)	4.5 nm	500°C
RuO_2 (20%)	4.5 nm	550°C

7.2 RuO_2 sputtering

Based on the values for RuO_2 and Ru from section 7, resistivity and thickness tests were made for the different oxygen ratios of the Ru bottom electrode.
Low magnetron power and a variation of oxygen pressure during sputtering should provide a low resistivity according to [51] where they mention , ideal for an electrode as we want the voltage drop to be over the ferroelectric film. One test using the parameters 100 W and 50% O_2[54]was done to attempt to emulate the low resistivity value of $< 100\mu\Omega cm$ as well as several tests using the more recent, optimal sputtering conditions of 60 W and 0-20% O_2[51].
The process had not been previously done with the sputtering tool available, so the conditions were naturally different from the ones used in the mentioned articles. 75 W was used instead of 60 W because of the inability to hold a stable plasma at lower power, and 20 sccm Ar was the maximum as opposed to 30 sccm. Using the conditions available, five tests were made. Refer to table 2.

Table 2: Parameters of the Ru and RuO_2 sputtering test samples.

75 W	75 W 10% O_2	75 W 20% O_2	75 W 30% O_2	100 W 50% O_2

The approximate thickness results are seen in table 3. The TiN BE was of 10 nm thickness,

but unfortunately because of the $Ru(O_2)$ sputtering process being new and the growth rate not yet fully known, the $Ru(O_2)$ BE's are not of the same thickness. This may play a part in the further analysis of these samples.

Table 3: Approximate thicknesses of the Ru and RuO_2 samples.

75 W	75 W 10% O_2	75 W 20% O_2	75 W 30% O_2	100 W 50% O_2
19 nm	33 nm	37 nm	42 nm	29 nm

Table 4: Approximate resistivities of the Ru and RuO_2 samples.

75 W	75 W 10% O_2	75 W 20% O_2	75 W 30% O_2	100 W 50% O_2
50 $\mu\Omega cm$	400 $\mu\Omega cm$	480 $\mu\Omega cm$	550 $\mu\Omega cm$	404 $\mu\Omega cm$

These values are higher than the reported values, but not with several magnitudes so the films will be considered to still be useable. The differing values most likely indicate that the issues lie somewhere within the admittedly un-optimised process of sputtering RuO_2 with the tool available in the lab and/or human error. Further work may investigate higher power and low range of oxygen content to further improve the resistance of RuO_2. For Ru, higher power may also result in lower resistivity.

7.3 10 nm HZO

The PUND measurements for the 10 nm FTJ's with TiN, Ru, and RuO_2 as bottom electrodes can be seen in fig.10, fig.11, and fig.12 respectively. Whilst the TiN and Ru samples underwent a 2.5V cycling, RuO_2 (20%) needed 3V cycles to saturate the polarisation. The reason for a higher voltage for the oxide might be because it needs to overcome the built-in field the work function difference provides.

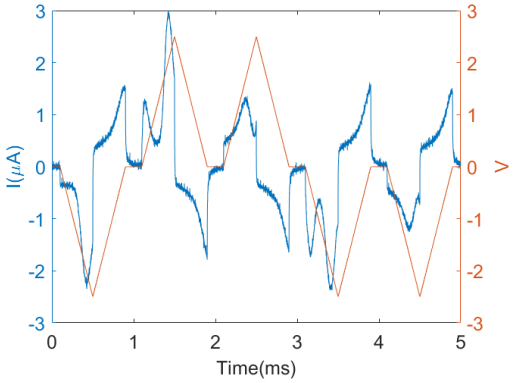

(a) PUND of 10 nm FTJ with TiN bottom electrode in pristine condition.

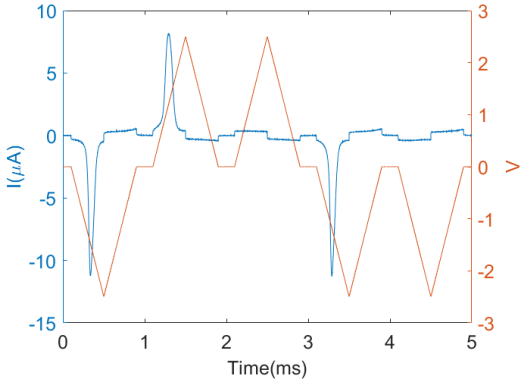

(b) PUND of 10 nm FTJ with TiN bottom electrode in after 20k cycles.

Figure 10: PUND measurements of the TiN bottom electrode sample.

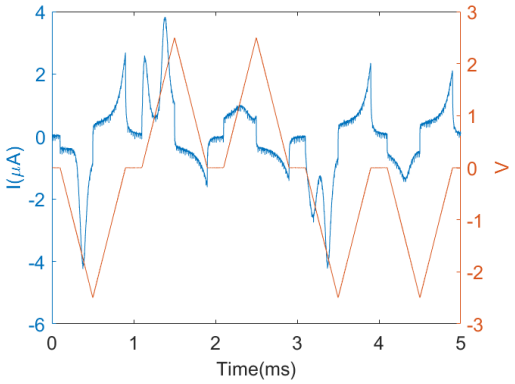

(a) PUND of 10 nm FTJ with Ru bottom electrode in pristine condition.

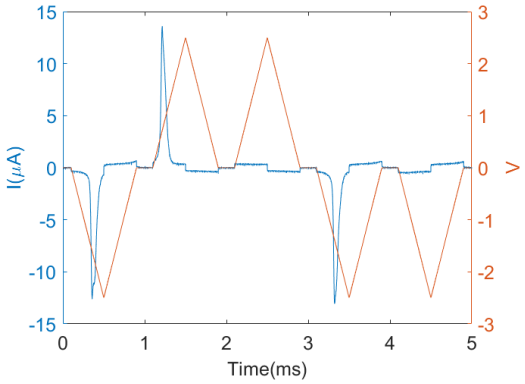

(b) PUND of 10 nm FTJ with Ru bottom electrode in after 20k cycles.

Figure 11: PUND measurements of the Ru bottom electrode sample.

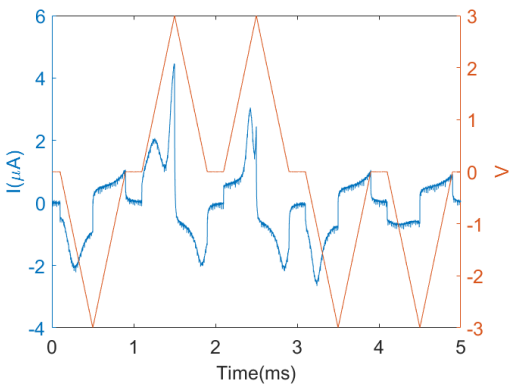

(a) PUND of 10 nm FTJ with RuO_2 (20%) bottom electrode in pristine condition.

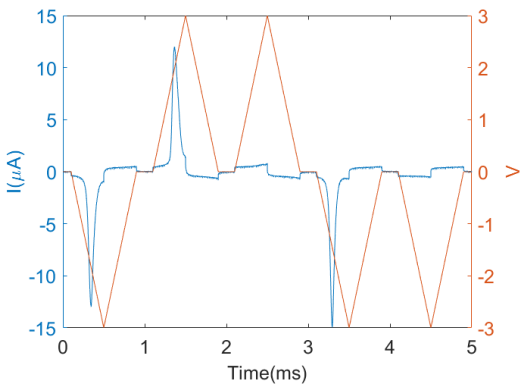

(b) PUND of 10 nm FTJ with RuO_2 (20%) bottom electrode in after 20k cycles.

Figure 12: PUND measurements of the RuO_2 (20%) bottom electrode sample.

The results of these show quite similar results between the different bottom electrodes. In the pristine states, it can be clearly seen that the samples are not fully woken up as there are switching current peaks at the second identical switching pulses (the UP and DOWN pulses). This means that all of the domains do not fully align initially. There are also switching current peaks in the opposite direction immediately after the pulses, showing that some of the domains switch back. All of these devices show this behaviour, as well as removing any of that behaviour after being cycled. The only remaining currents during the other pulses are leakage and capacitive currents.

Figure.13 shows the PE hysteresis curves of the three devices at different levels of cycling. The initial pristine state shows a poor hysteresis shape, with the polarisation not increasing or decreasing linearly with the electric field. As is consistent with the previous PUND plots, the ferroelectricity grows with the amount of wake-up cycles, as well as evening out the non-linear relationship between the polarisation and the electric field at the pristine state. The TiN sample shows 42 $\mu C/cm^2$, consistent with previously reported values at around $45\mu C/cm^2$ after cycling. Considering neither the TiN nor Ru samples are fully woken up as can be seen in fig.14, it is likely that the TiN sample will reach this reported value and might even surpass Ru if cycled long enough. It can also be seen that both the Ru and RuO_2 samples show a larger remnant polarisation than the TiN, with RuO_2 having the largest $2P_r$ at around 55 $\mu C/cm^2$. This is consistent with the theory that a lower CTE leads to higher ferroelectricity.

The plots show a strong ferroelectric response at a relatively low annealing temperature of 500°C. Whilst the coercive electric field E_c (the field strength for when the polarisation switches) for the TiN sample is -1.1 V and 1.2 V and thus relatively symmetric around the y axis (at zero E_c), the Ru and RuO_2 samples are not. They have E_c values of around -0.8 V to 1.5 V and -2 V to 1.3 V respectively. Since it has been reported that an asymmetry in the E_c is caused by work function differences[37], it makes sense that the E_c is shifted since there is a larger work function difference for Ru and RuO_2. Although bound charges at the interface, including oxygen

vacancies, have also been reported to cause E_c asymmetry[41]. This should be of lesser impact than the work function difference since the Ru and RuO_2 samples should theoretically have fewer oxygen vacancies.

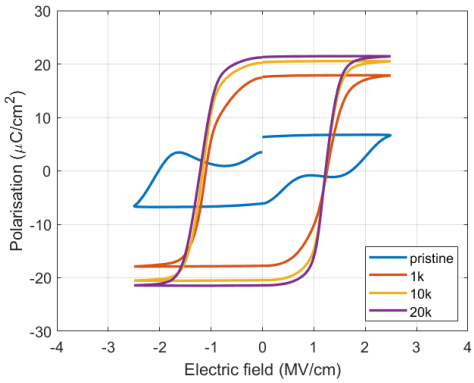

(a) PE of 10 nm HZO FTJ with TiN bottom electrode.

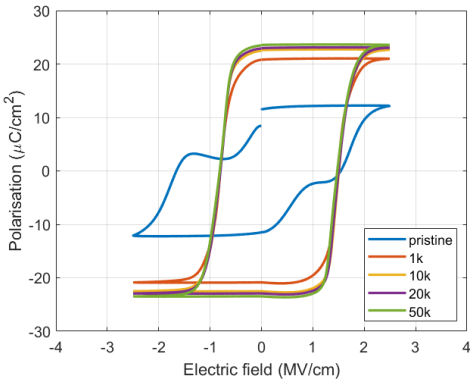

(b) PE of 10 nm HZO FTJ with Ru bottom electrode.

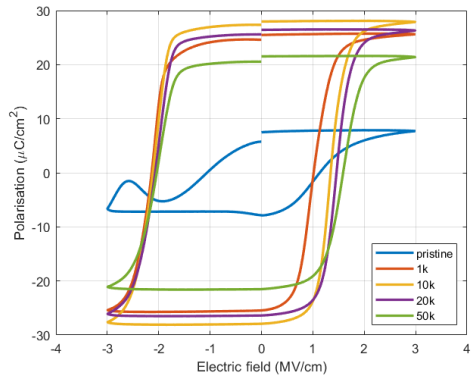

(c) PE of 10 nm HZO FTJ with RuO_2 (20%) bottom electrode.

Figure 13: Polarisation vs electric field plots of the three FTJ's at different cycles.

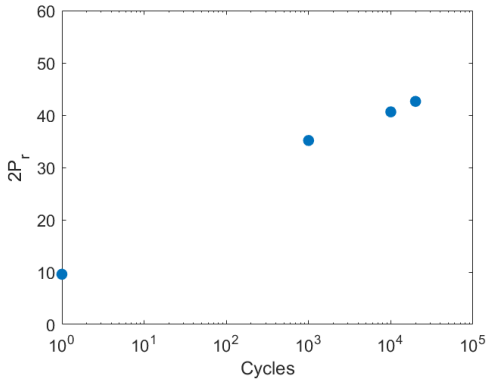

(a) Endurance of 10 nm HZO FTJ with TiN bottom electrode.

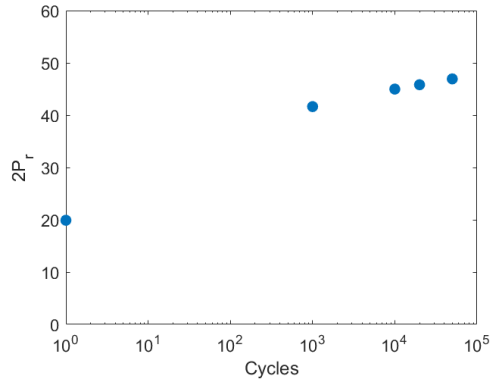

(b) Endurance of 10 nm HZO FTJ with Ru bottom electrode.

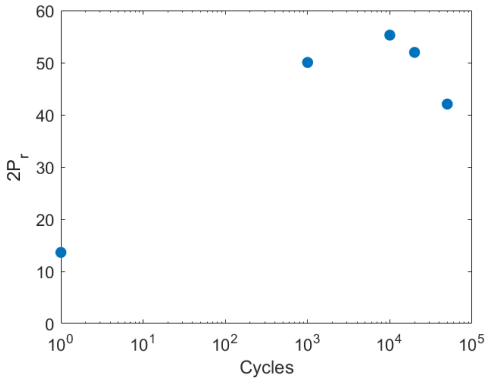

(c) Endurance of 10 nm HZO FTJ with RuO_2 (20%) bottom electrode.

Figure 14: Remnant polarisation versus amount of cycles. Shows the endurance of the HZO film.

By plotting the $2P_r$ versus the cycles in fig.14, we can see a clear behaviour of how the devices fare after certain amounts of cycling. TiN shows no sign of fatigue after 20k cycles, neither does Ru, although it seems to saturate earlier than TiN, opening up the possibility of TiN to overtake Ru when fully saturated. RuO_2 however, shows fatigue at 20k cycles, decreasing its $2P_r$ at 50k cycles. This seems to point towards RuO_2 at 20% oxygen not fulfilling its primary function of an oxygen vacancy sink for 10 nm HZO films, but it could also be the case that the RuO_2 sample being cycled at a slightly higher voltage.
Fig.15 shows the IV characteristics of the three FTJ's, and the fatigue behaviour of RuO_2 can be seen as the switching current decreases with the amount of cycles. The reasoning for not cycling more was that at this point the main focus was seeing if the Ru and RuO_2 samples could show proper ferroelectricity.

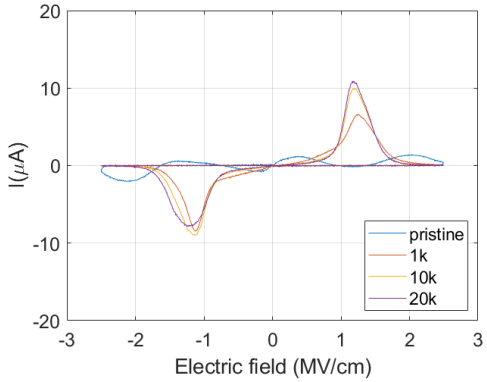

(a) IV of 10 nm HZO FTJ with TiN bottom electrode.

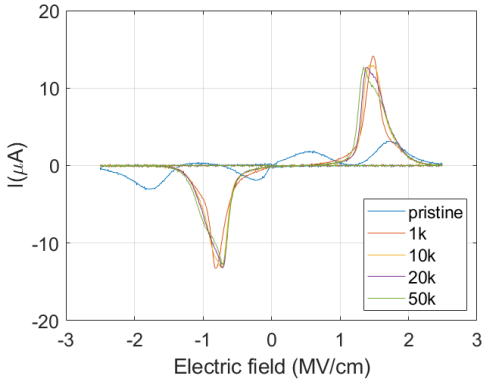

(b) IV of 10 nm HZO FTJ with Ru bottom electrode.

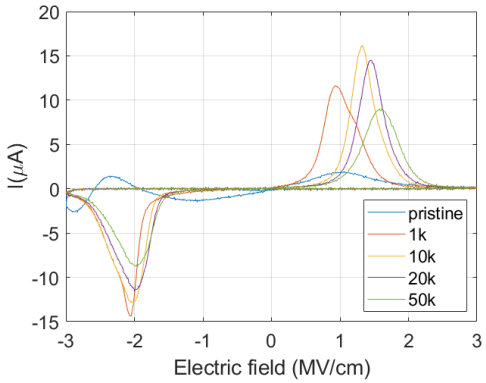

(c) IV of 10 nm HZO FTJ with RuO_2 (20%) bottom electrode.

Figure 15: IV characteristics of the three FTJ's at different cycles.

7.4 6 nm HZO

Decreasing the thickness of the ferroelectric layer in an FTJ is crucial to obtain a sufficient current. Following that condition however comes some detrimental effects such as additional leakage current, potentially worse E_c asymmetry[41], and lower polarisation[38].

One thing to note is that during the sputtering of the W TE on the 500°C sample, the W source was placed in a different magnetron position than the default one, making the tooling factor of the sputterer's thickness meter incorrect. This lead to an unknown, most likely thicker thickness, and was taken to the profilometer for measuring. There was no obvious step to measure on, so multiple "good-enough" measurements were taken and they were in the range of 20-100 nm. This was deemed good enough for measuring but could of course be a factor in any further result, as a thicker top electrode provides more tensile stress[48]. Additionally, both the 500°C and 550°C samples used for these measurements underwent certain issues during fabrication, and many devices on them were deemed unusable for measuring. One issue was that the W was not

properly lifted off from all samples. Another being that some remaining resist melted during annealing, leaving behind traces that could impede probing the devices. The Ru samples was cycled between -2 to 2 V. The RuO_2 sample here was cycled between -4 to 4 V but wake-up at -2 to 2 V, as it broke down if cycled at -4 to 4 V. Preferably you want to keep the same voltage, as the lower voltage cycles have a lesser impact.

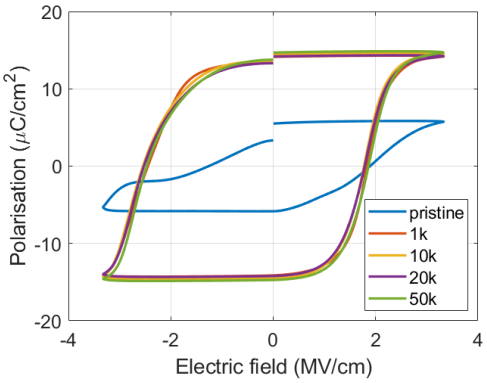

(a) PE of 6 nm HZO FTJ with Ru BE at 500°C.

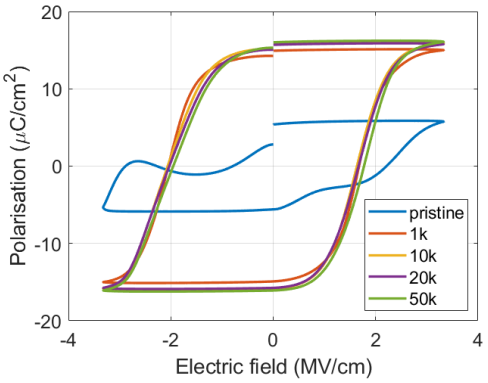

(b) PE of 6 nm HZO FTJ with Ru BE at 550°C.

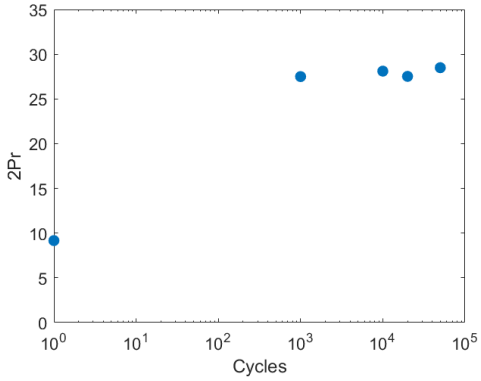

(c) Endurance of 6 nm HZO with Ru BE at 500°C.

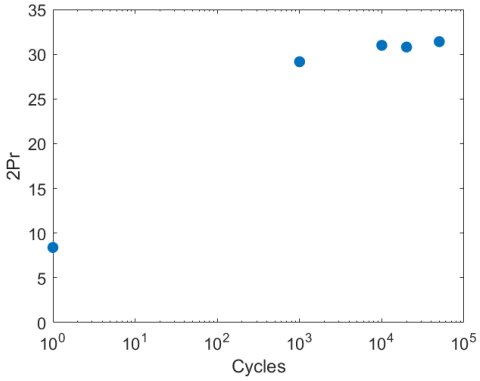

(d) Endurance of 6 nm HZO with Ru BE at 550°C.

Figure 16: Polarisation vs electric field and endurance plots with Ru BE at different annealing temperatures.

The results from these samples agree with theory as the decrease in FE film thickness decreases the polarisation and increases the coercive field, and increased annealing temperature increases the polarisation, going from $29\mu C/cm^2$ to $32\mu C/cm^2$. They also show a similar saturation of the polarisation after 1k cycles, implying that the HZO has fully woken up, although considering that the wake-up cycles were not at 4 V it may be premature to declare that the HZO has woken up fully. There is no sign of fatigue after 50k cycles.

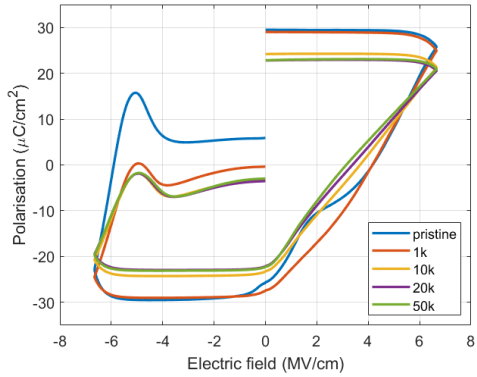

(a) PE of 6 nm HZO FTJ with RuO_2 (20%) BE at an annealing temperature of 500°C.

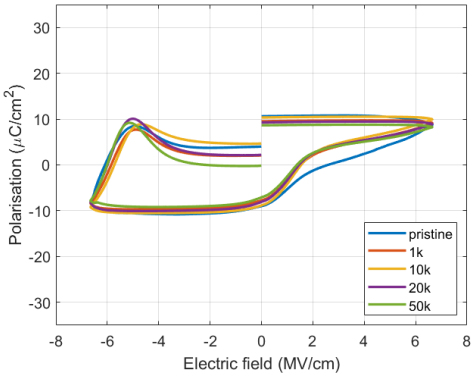

(b) PE of 6 nm HZO FTJ with RuO_2 (20%) BE at an annealing temperature of 550°C.

Figure 17: Polarisation vs electric field plot with RuO_2 (20%) BE at different annealing temperatures.

Fig.17a shows clear mismatches in the hysteresis curves at the remnant polarisations. It is unclear whether this is a fabrication issue or not. The E_c has been shifted to a point where the polarisation starts switching immediately after the electric field changes sign. Further analysis of this data can be done by looking at the PUND measurements of this device.

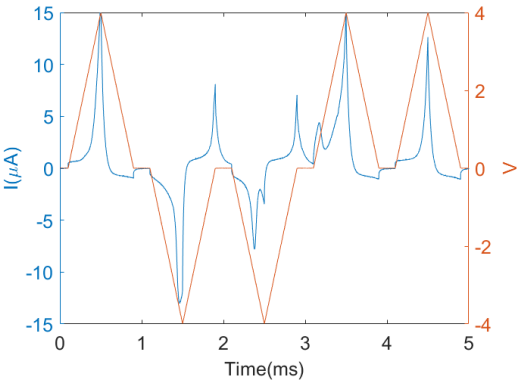

(a) Pristine PUND.

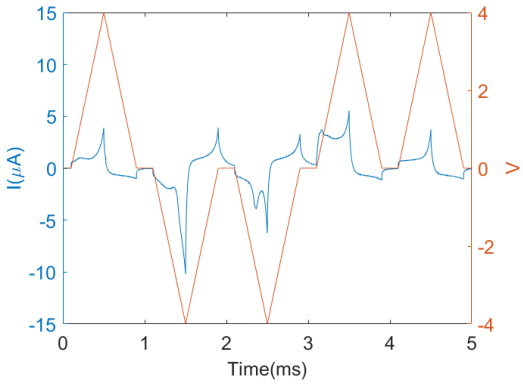

(b) PUND after 50k cycles shows similar behaviour.

Figure 18: PUND for RuO_2 (20%) at 500°C.

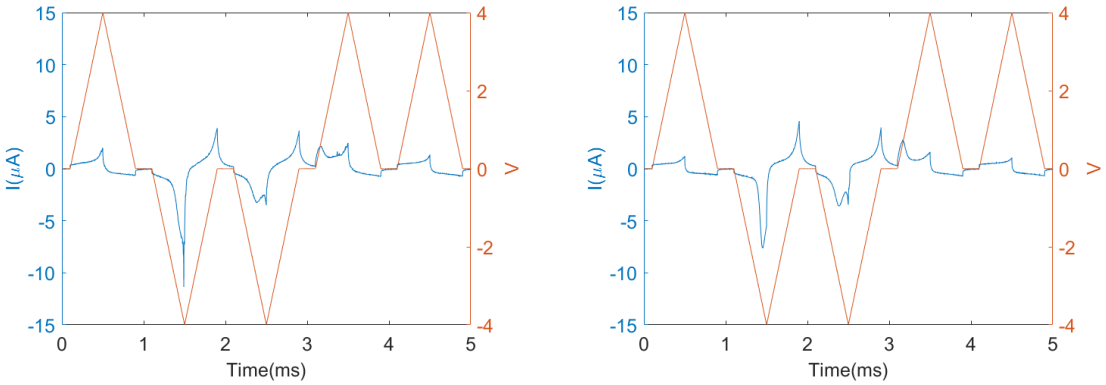

(a) Pristine PUND.

(b) PUND after 50k cycles shows similar behaviour.

Figure 19: PUND for RuO_2 (20%) at 550°C.

After the Positive pulse we see some re-polarisation. So during the Up pulse, there is once again polarisation. When subtracting the Up pulse from the Positive pulse as stated in chapter 6.5.3, we subtract a part of the polarisation before integrating it.
After the Up pulse there is re-polarisation again. When the switch to the Negative pulse comes along, there is already some polarisation in that direction meaning that there will be a smaller polarisation current. This, combined with that there is no re-polarisation from the negative pulses, means that there will be a large gap in polarisation when going from positive to negative voltage as can clearly be seen in fig.17. The real $2P_r$ value is thus not clearly known because of these faults.

7.5 4.5 nm HZO

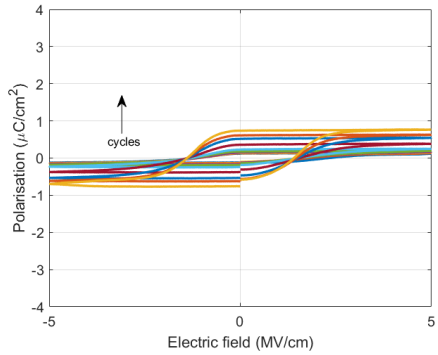

(a) 4.5 nm HZO with TiN BE annealed at 500°C.

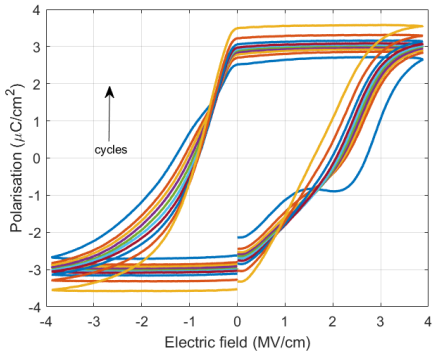

(b) 4.5 nm HZO with TiN BE annealed at 550°C.

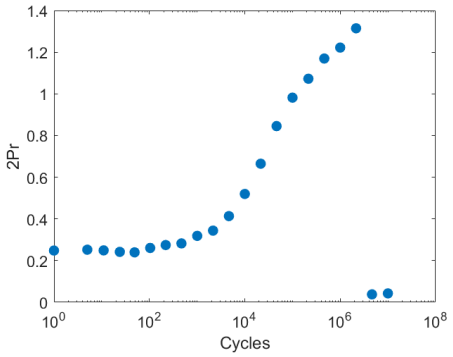

(c) Endurance of the 4.5 nm HZO layer for 500°C.

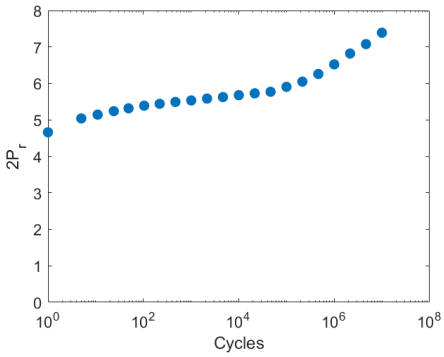

(d) Endurance of the 4.5 nm HZO layer for 550°C.

Figure 20: 4.5 nm HZO with TiN BE with comparisons of 500-550°C annealing temperatures.

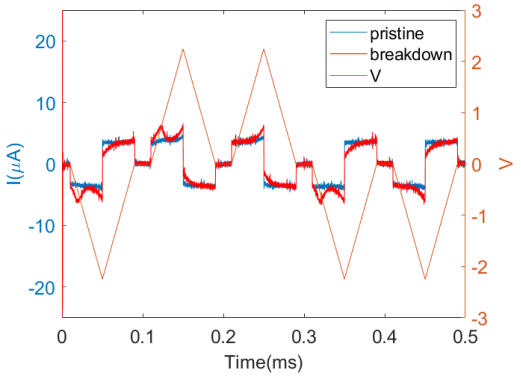

(a) PUND

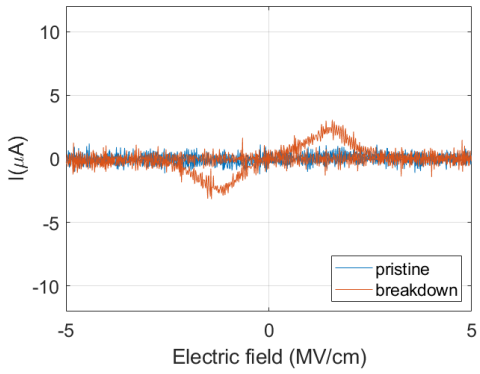

(b) IV

Figure 21: PUND and IV measurements taken at the pristine condition as well as right before breakdown of the 4.5 nm HZO TiN BE annealed at 500°C.

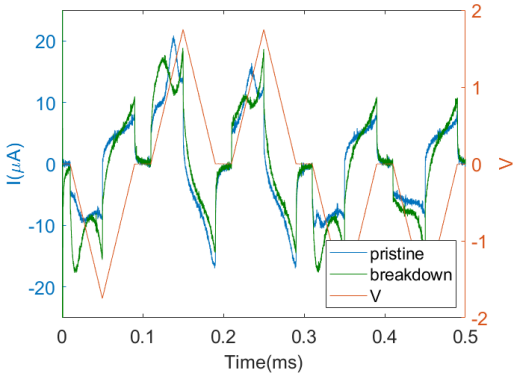

(a) PUND

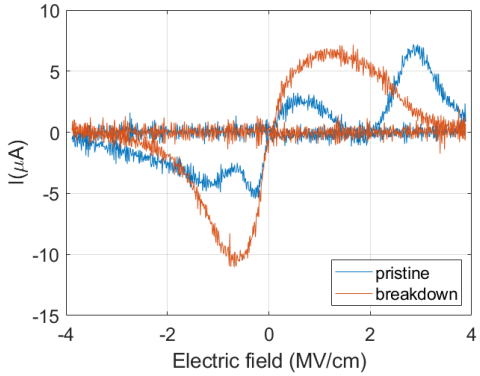

(b) IV

Figure 22: PUND and IV measurements taken at the pristine condition as well as right before breakdown of the 4.5 nm HZO TiN BE annealed at 550°C.

The reference sample of W/HZO/TiN shows negligible ferroelectricity at 500°C as well as breaking down completely at around 10^6 cycles. Increasing the annealing temperature to 550°C increases the polarisation to around $3.5\mu C/cm^2$. This value is close to reported values of $5\mu C/cm^2$ at 5 nm, however that sample was annealed at 500°C[60]. Looking at fig.20d, the film seems to not even have fully woken up yet, even at 10^7 cycles.

Fig.21 and 22 shows the PUND and IV plots at pristine condition as well as right before the devices broke (or at the last measured cycle in the 550°C case). Fig.21 shows low polarisation currents although right before breakdown there is a tiny polarisation peak, showing some improvement from the pristine condition. Fig.22 shows more promising results. An interesting thing to note for these TiN based samples is that they now show a strong E_c shift, possibly linking it

to defects since the work function difference is small.

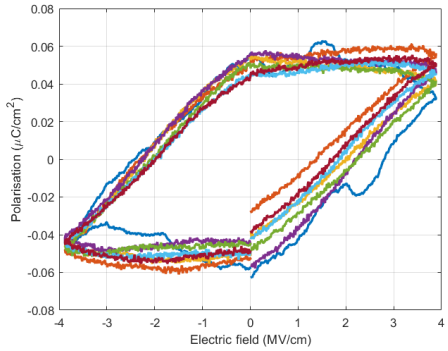

(a) 4.5 nm HZO with Ru BE annealed at 500°C.

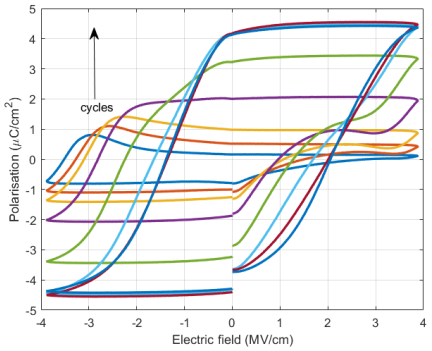

(b) 4.5 nm HZO with Ru BE annealed at 550°C.

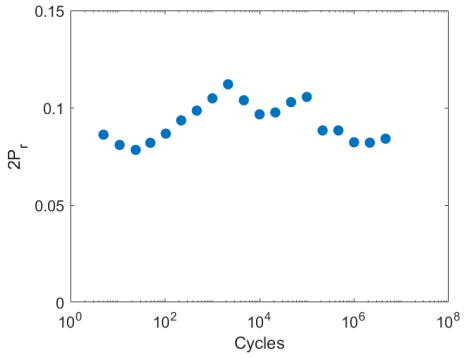

(c) Endurance of the 4.5 nm HZO layer with Ru BE for 500°C.

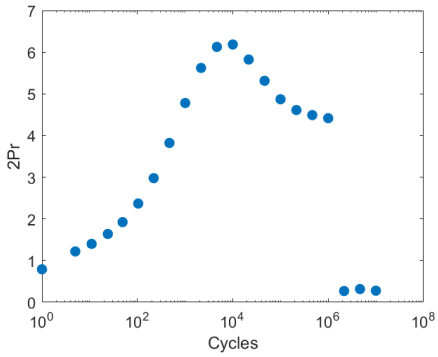

(d) Endurance of the 4.5 nm HZO layer with Ru BE for 550°C.

Figure 23: 4.5 nm HZO with Ru BE with comparisons of 500-550°C annealing temperatures.

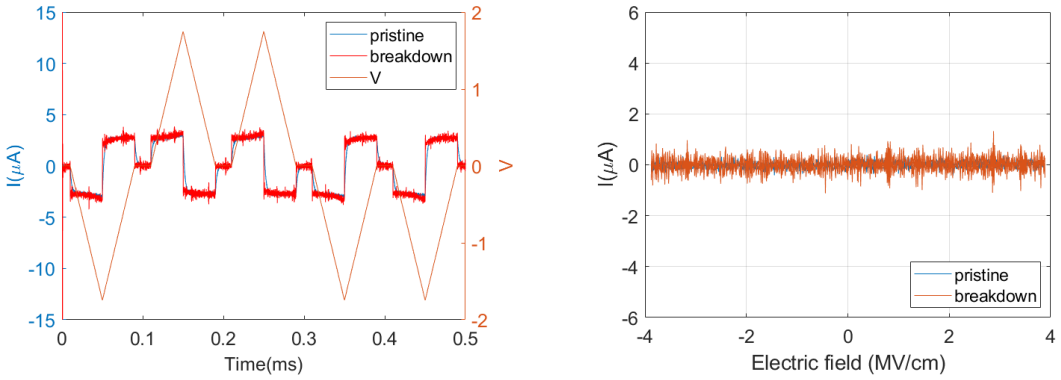

(a) PUND (b) IV

Figure 24: PUND and IV measurements taken at the pristine condition as well as right before breakdown of the 4.5 nm HZO Ru BE annealed at 500°C.

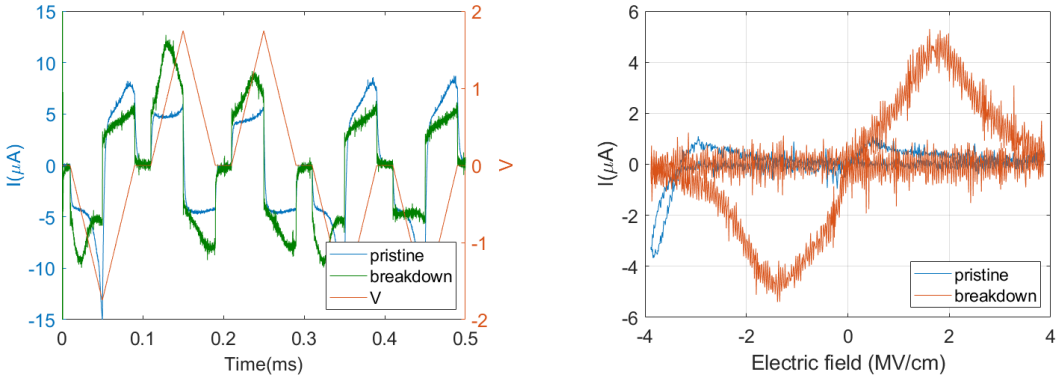

(a) PUND (b) IV

Figure 25: PUND and IV measurements taken at the pristine condition as well as right before breakdown of the 4.5 nm HZO Ru BE annealed at 550°C.

Returning to Ru as the bottom electrode, 4.5 nm HZO at 500°C shows barely any ferroelectricity even after heavy cycling. This follows the same pattern as for the TiN sample at the same temperature. For the 550°C sample however, the ferroelectricity wakes up and grows to a $2P_r$ of around $8\mu C/cm^2$ where it is fully woken up but breaks down swiftly at around 10^5 cycles. The coercive field decreases with an increase in cycles as well, not being consistent with the behaviour of the Ru BE at either 10 or 6 nm. Fig.24 shows only noise in the IV plot, no polarisation current in sight. The hysteresis in fig.23a must then be because a dielectric polarisation or some trapped charges.

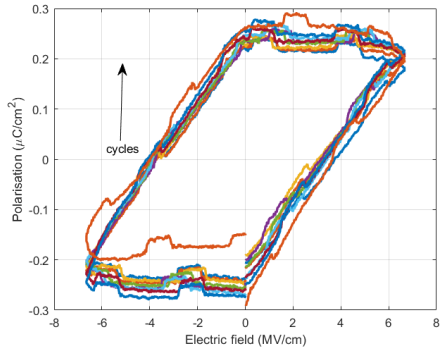

(a) 4.5 nm HZO with RuO_2 (10%) BE annealed at 500°C.

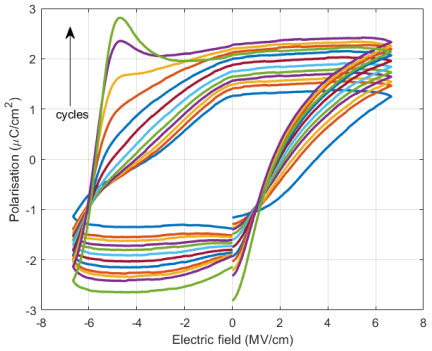

(b) 4.5 nm HZO with RuO_2 (10%) BE annealed at 550°C.

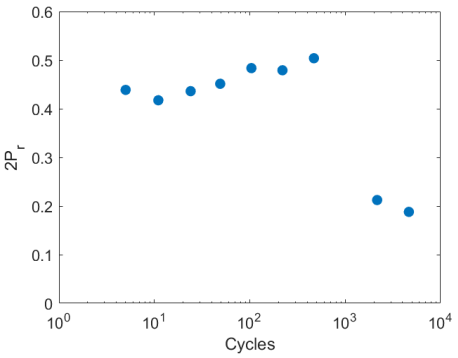

(c) Endurance of the 4.5 nm HZO layer with RuO_2 (10%) BE for 500°C.

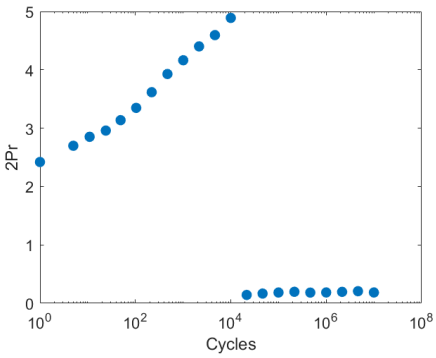

(d) Endurance of the 4.5 nm HZO layer with RuO_2 (10%) BE for 550°C.

Figure 26: 4.5 nm HZO with RuO_2 (10%) BE with comparisons of 500-550°C annealing temperatures.

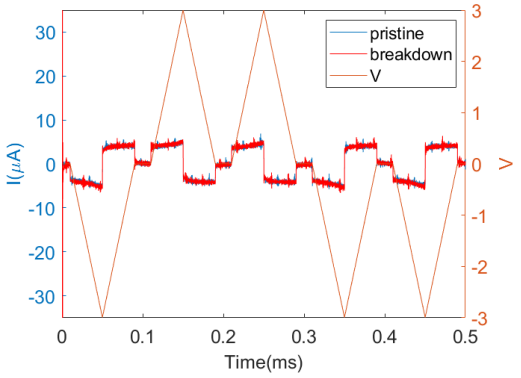

(a) PUND

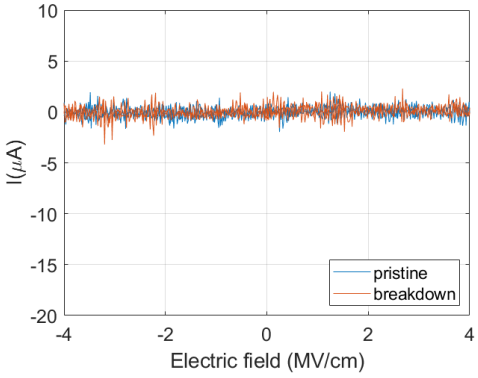

(b) IV

Figure 27: PUND and IV measurements taken at the pristine condition as well as right before breakdown of the 4.5 nm HZO RuO_2 (10%) BE annealed at 500°C.

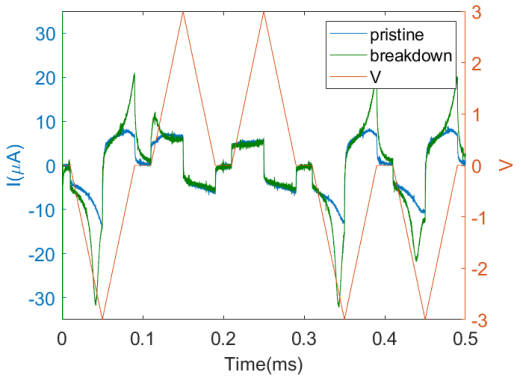

(a) PUND

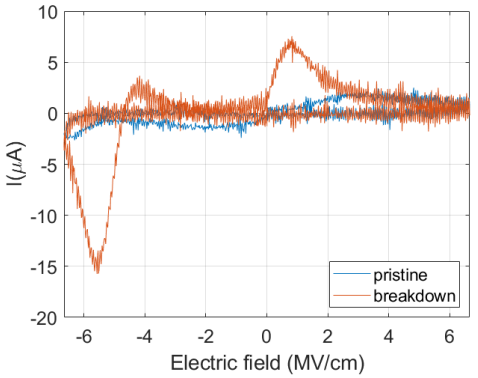

(b) IV

Figure 28: PUND and IV measurements taken at the pristine condition as well as right before breakdown of the 4.5 nm HZO RuO_2 (10%) BE annealed at 550°C.

There is negligible ferroelectricity in the sample annealed at 500°C. Increasing the annealing temperature however shows traces of ferroelectricity, although weak.

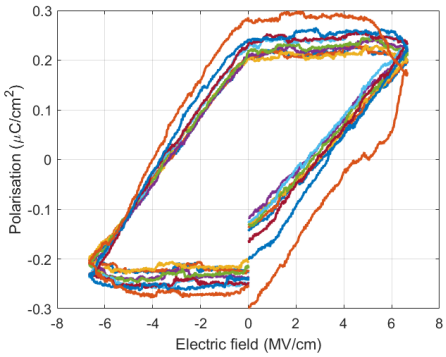

(a) 4.5 nm HZO with RuO_2 (20%) BE annealed at 500°C.

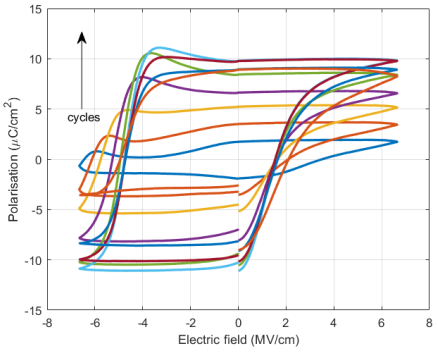

(b) 4.5 nm HZO with RuO_2 (20%) BE annealed at 550°C.

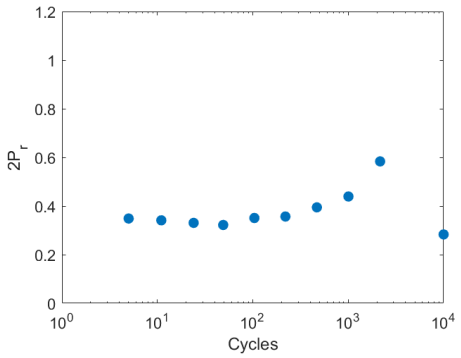

(c) Endurance of the 4.5 nm HZO layer with RuO_2 (20%) BE for 500°C.

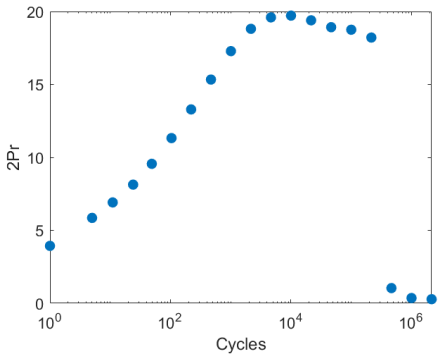

(d) Endurance of the 4.5 nm HZO layer with RuO_2 (20%) BE for 550°C.

Figure 29: 4.5 nm HZO with RuO_2 (20%) BE with comparisons of 500-550°C annealing temperatures.

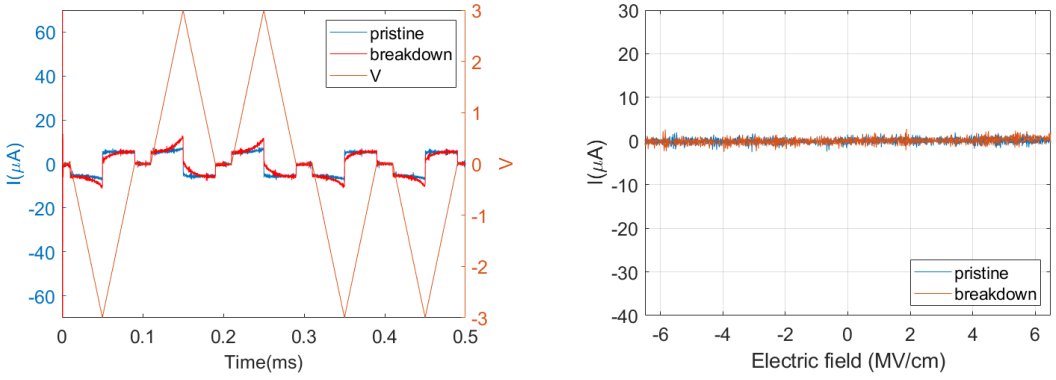

(a) PUND (b) IV

Figure 30: PUND and IV measurements taken at the pristine condition as well as right before breakdown of the 4.5 nm HZO RuO_2 (20%) BE annealed at 500°C.

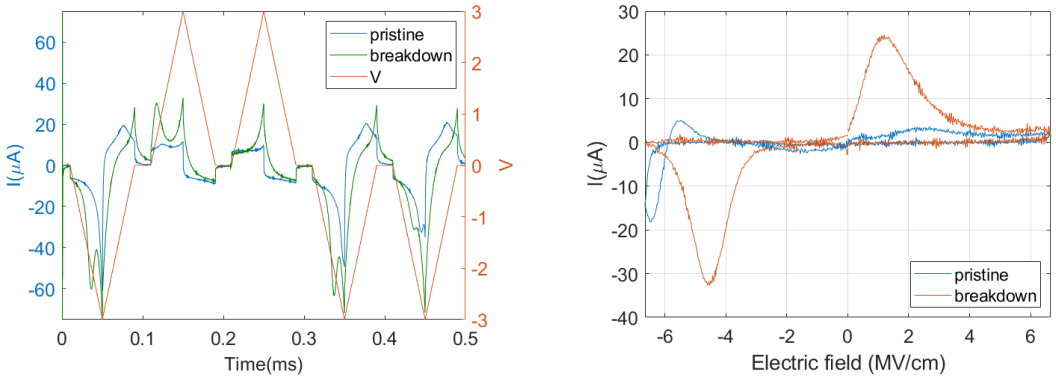

(a) PUND (b) IV

Figure 31: PUND and IV measurements taken at the pristine condition as well as right before breakdown of the 4.5 nm HZO RuO_2 (20%) BE annealed at 550°C

Once again there is basically no ferroelectricity at 500°C, but there is a good ferroelectric response at 550°C with a great $2P_r$ of $20\mu C/cm^2$. Its endurance shows more potential than the RuO_2 (10%) sample at 550°C, which together with the increased polarisation shows promise in the higher oxygen ratio RuO_2 electrode.

8 Conclusions

To summarise, a study on the potential use for Ru and RuO_2 as bottom electrodes for ultrathin HZO FTJ's were conducted.

With $Ru(O_2)$ sputtering being a new process in LNL, parameters taken from various publications were used to make sufficient bottom electrodes. Their resistivities were measured to compare to optimal values of $<100\mu\Omega$cm. Obtaining values ranging from $49.7\mu\Omega$cm for the pure Ru to $546\mu\Omega$cm for the RuO_2 with 30% oxygen, the values were deemed sufficient. Followed were PUND measurements, from which PUND, PE, IV, and endurance plots were made. Results showed RuO_2 as having the best $2P_r$ value at 10 nm with $55\mu C/cm^2$, although cycled at a higher field. Decreasing the FE thickness to 6 nm, Ru BE shows clear PE improvements with a $2P_r$ of around $32\mu C/cm^2$ when annealed at 550°C as opposed to around $28\mu C/cm^2$ for 500°C, consistent with theory. The samples with the RuO_2 (20%) BE at 6 nm showed large offsets in their PE plots because of re-polarisation. Decreasing the FE thickness further to 4.5 nm, all samples annealed at 500°C stop showing signs of ferroelectricity, with the 550°C samples showing only weak signs, except for RuO_2 (20%) which shows an excellent $2P_r$ of $20\mu C/cm^2$, but with room to improve with an endurance of around $2{\cdot}10^5$. This result makes it the most worthwhile contender for a BE at lower thickness out of the ones tested.
The thesis topic could be expanded in many ways. The RuO_2 sputtering process could be optimised and its crystalline structure verified to achieve the best possible electrode. The tests run on the devices could undergo a wider range of parameters to pinpoint the edge cases, allowing us to hone in on the optimal temperature/thickness/oxygen ratio values.

References

[1] Kim SJea. Low-voltage operation and high endurance of 5-nm ferroelectric HF0.5zr0.5O2 capacitors. Applied Physics Letters. 2018;113(18).

[2] The Trustees of Princeton University;. Available from: `https://press.princeton.edu/ideas/is-the-human-brain-a-biological-computer`.

[3] Valasek J. Piezo-electric and allied phenomena in Rochelle Salt. Physical Review. 1921;17(4):475–481.

[4] Setter N, Damjanovic D, Eng L, Fox G, Gevorgian S, Hong S, et al. Ferroelectric thin films: Review of materials, properties, and applications. Journal of Applied Physics. 2006;100(5):051606.

[5] Böscke T, Müller J, Bräuhaus D, Schröder U, Böttger U. Ferroelectricity in hafnium oxide thin films. Applied Physics Letters. 2011;99(10):102903.

[6] Müller J, Böscke TS, Schröder U, Mueller S, Bräuhaus D, Böttger U, et al. Ferroelectricity in Simple Binary ZrO2 and HfO2. Nano Letters. 2012;12(8):4318-23. PMID: 22812909. Available from: `https://doi.org/10.1021/nl302049k`.

[7] Goh Y, Cho SH, Park SHK, Jeon S. Oxygen vacancy control as a strategy to achieve highly reliable hafnia ferroelectrics using oxide electrode. Nanoscale. 2020;12:9024-31. Available from: `http://dx.doi.org/10.1039/D0NR00933D`.

[8] Wright WJ, Askeland DR. The Science and Engineering of Materials. 7th ed. Cengage; 2022.

[9] Florent K. Ferroelectric HfO2 for Emerging Ferroelectric Semiconductor Devices Devices; 2015.

[10] Littlewood P. Physics of ferroelectrics; 2002. http://www.tcm.phy.cam.ac.uk/âĹijpbl21/ferroelectrics/ferro.pdf.

[11] Catalan G, Scott JF, Schilling A, Gregg JM. Wall thickness dependence of the scaling law for ferroic stripe domains. Journal of Physics: Condensed Matter. 2006 dec;19(2):022201. Available from: https://dx.doi.org/10.1088/0953-8984/19/2/022201.

[12] Centore R. Special Issue "Polar and Centrosymmetric Packings in Molecular Crystals"; 2017.

[13] Havir H. Growth and Characterization of Ferroelectric Lanthanum-DopedHafnia; 2020.

[14] Park MH, Lee YH, Kim HJ, Kim YJ, Moon T, Kim KD, et al. Ferroelectricity and antiferroelectricity of doped thin HFO2-based films. Advanced Materials. 2015;27(11):1811–1831.

[15] Hao X, Zhai J, Kong LB, Xu Z. A comprehensive review on the progress of lead zirconate-based antiferroelectric materials. Progress in Materials Science. 2014;63:1-57. Available from: https://www.sciencedirect.com/science/article/pii/S0079642514000127.

[16] Wang X, Zhu Q, Sun H, Wang M, Xu R, Feng Y, et al. Ultrahigh energy storage density and efficiency in PLZST antiferroelectric ceramics via multiple optimization strategy. Journal of the European Ceramic Society. 2023;43(9):4051–4059.

[17] Pantel D, Alexe M. Electroresistance effects in ferroelectric tunnel barriers. Phys Rev B. 2010 Oct;82:134105. Available from: https://link.aps.org/doi/10.1103/PhysRevB.82.134105.

[18] Esaki aL, Laibowitz R, Stiles P. Polar switch. IBM Tech Discl Bull. 1971;13(2161):114.

[19] Zhuravlev MY, Sabirianov RF, Jaswal SS, Tsymbal EY. Giant Electroresistance in Ferroelectric Tunnel Junctions. Phys Rev Lett. 2005 Jun;94:246802. Available from: https://link.aps.org/doi/10.1103/PhysRevLett.94.246802.

[20] Garcia V, Bibes M. Ferroelectric tunnel junctions for information storage and processing. Nat Commun. 2014;5(4289).

[21] Gruverman A, Wu D, Lu H, Wang Y, Jang HW, Folkman CM, et al. Tunneling Electroresistance Effect in Ferroelectric Tunnel Junctions at the Nanoscale. Nano Letters. 2009;9(10):3539-43. PMID: 19697939. Available from: https://doi.org/10.1021/nl901754t.

[22] Ryu H, Wu H, Rao F, Zhu W. Ferroelectric tunneling junctions based on aluminum oxide/zirconium-doped hafnium oxide for neuromorphic computing. Scientific Reports. 2019;9(1).

[23] Kobayashi M, Tagawa Y, Mo F, Saraya T, Hiramoto T. Ferroelectric HfO2 Tunnel Junction Memory With High TER and Multi-Level Operation Featuring Metal Replacement Process. IEEE Journal of the Electron Devices Society. 2019;7:134-9.

[24] Siannas N, Zacharaki C, Tsipas P, Chaitoglou S, Bégon-Lours L, Istrate C, et al. Metastable ferroelectricity driven by depolarization fields in Ultrathin hf0.5zr0.5o2. Communications Physics. 2022;5(1).

[25] Athle R. Development of Ferroelectric HafniumOxide for Negative Capacitance FieldEffect Transistors; 2019.

[26] Strukov DB, Snider GS, Stewart DR, Williams RS. The missing memristor found. Nature. 2008;453(7191):80–83.

[27] Chanthbouala A, Garcia V, Cherifi RO, Bouzehouane K, Fusil S, Moya X, et al. A ferroelectric memristor. Nature Materials. 2012;11(10):860–864.

[28] Yang R. In-memory computing with ferroelectrics. Nature Electronics. 2020;3(5):237–238.

[29] Shiraishi T, Katayama K, Yokouchi T, Shimizu T, Oikawa T, Sakata O, et al. Impact of mechanical stress on ferroelectricity in (HF0.5zr0.5)o2 thin films. Applied Physics Letters. 2016;108(26):262904.

[30] Hubbard KJ, Schlom DG. Thermodynamic stability of binary oxides in contact with silicon. Journal of Materials Research. 1996;11(11):2757–2776.

[31] Warusawithana MP, Cen C, Sleasman CR, Woicik JC, Li Y, Kourkoutis LF, et al. A ferroelectric oxide made directly on silicon. Science. 2009;324(5925):367–370.

[32] Thean A, Tsai SH, Chen CK, Sivan M, Tang B, Hooda S, et al. Low-thermal-budget beol-compatible beyond-silicon transistor technologies for future monolithic-3d compute and memory applications. 2022 International Electron Devices Meeting (IEDM). 2022.

[33] Kim SJ, Mohan J, Lee J, Lee JS, Lucero AT, Young CD, et al. Effect of film thickness on the ferroelectric and dielectric properties of low-temperature (400°C) HF0.5zr0.5O2 films. Applied Physics Letters. 2018;112(17):172902.

[34] Hyuk Park M, Joon Kim H, Jin Kim Y, Moon T, Seong Hwang C. The effects of crystallographic orientation and strain of thin HF0.5zr0.5O2 film on its ferroelectricity. Applied Physics Letters. 2014;104(7):072901.

[35] Park MH, Kim HJ, Kim YJ, Lee YH, Moon T, Kim KD, et al. Study on the size effect in HF0.5zr0.5O2 films thinner than 8nm before and after wake-up Field Cycling. Applied Physics Letters. 2015;107(19):192907.

[36] Asapu S, Pagaduan JN, Zhuo Y, Moon T, Midya R, Gao D, et al. Large remnant polarization and great reliability characteristics in W/HZO/W ferroelectric capacitors. Frontiers in Materials. 2022;9.

[37] Athle R, Persson AEO, Troian A, Borg M. Top electrode engineering for freedom in design and implementation of ferroelectric tunnel junctions based on HF1–xZrxO2. ACS Applied Electronic Materials. 2022;4(3):1002–1009.

[38] Park MH, Lee YH, Kim HJ, Schenk T, Lee W, Kim KD, et al. Surface and grain boundary energy as the key enabler of ferroelectricity in Nanoscale Hafnia-Zirconia: A comparison of model and experiment. Nanoscale. 2017;9(28):9973–9986.

[39] Oh S, Kim H, Kashir A, Hwang H. Effect of dead layers on the ferroelectric property of Ultrathin HfZrOx film. Applied Physics Letters. 2020;117(25):252906.

[40] Liu B, Cao Y, Zhang W, Li Y. Excellent ferroelectric hf0.5zr0.5O2 thin films with ultra-thin al2O3 serving as capping layer. Applied Physics Letters. 2021;119(17).

[41] Zhu Y, Ning H, Yu Z, Pan Q, Zhang C, Luo C, et al. Thickness-dependent asymmetric potential landscape and polarization relaxation in ferroelectric $hf_xzr_{1+x}o$; thin films through interfacial bound charges. Advanced Electronic Materials. 2019;5(8).

[42] Dawber M, Chandra P, Littlewood PB, Scott JF. Depolarization corrections to the coercive field in thin-film ferroelectrics. Journal of Physics: Condensed Matter. 2003;15(24).

[43] Goh Y, Jeon S. The effect of the bottom electrode on ferroelectric tunnel junctions based on CMOS-compatible HFO2. Nanotechnology. 2018;29(33):335201.

[44] Lomenzo PDea. 'Ferroelectric HF1-XZrxO2 memories: Device reliability and depolarization fields'. 19th Non-Volatile Memory Technology Symposium (NVMTS). 2019.

[45] Libretexts. B1: Workfunction values (reference table);. Available from: `https://chem.libretexts.org/Ancillary_Materials/Reference/Reference_Tables/Bulk_Properties/B1%3A_Workfunction_Values_(Reference_Table)`.

[46] Vitale S, Kedzierski J, Healey P, Wyatt P, Keast C. Work-Function-Tuned TiN Metal Gate FDSOI Transistors for Subthreshold Operation. Electron Devices, IEEE Transactions on. 2011 03;58:419 426.

[47] Ťapajna M, Rosová A, Dobročka E, Štrbík V, Gaži Fröhlich K, et al. Work function thermal stability of RuO2-rich Ru–Si–O p-channel metal-oxide-semiconductor field-effect transistor gate electrodes. Journal of Applied Physics. 2008 04;103(7). 073702. Available from: `https://doi.org/10.1063/1.2901016`.

[48] Lee Y, Goh Y, Hwang J, Das D, Jeon S. The influence of top and bottom metal electrodes on ferroelectricity of Hafnia. IEEE Transactions on Electron Devices. 2021;68(2):523–528.

[49] Maiwa H, Ichinose N, Okazaki KOK. Preparation and Properties of Ru and RuO2 Thin Film Electrodes for Ferroelectric Thin Films. Japanese Journal of Applied Physics. 1994 sep;33(9S):5223. Available from: `https://dx.doi.org/10.1143/JJAP.33.5223`.

[50] Cao R, Liu Q, Liu M, Song B, Shang D, Yang Y, et al. Improvement of endurance in HZO-based ferroelectric capacitor using RU electrode. IEEE Electron Device Letters. 2019;40(11):1744–1747.

[51] Kim HK, Yu IH, Lee JH, Park TJ, Hwang CS. Controlling Work Function and Damaging Effects of Sputtered RuO2 Gate Electrodes by Changing Oxygen Gas Ratio during Sputtering. ACS Applied Materials & Interfaces. 2013;5(4):1327-32. PMID: 23384114. Available from: https://doi.org/10.1021/am302604e.

[52] Sawada T, Nabatame T, Dao TD, Yamamoto I, Kurishima K, Onaya T, et al. Improvement of smooth surface of RuO2 bottom electrode on Al2O3 buffer layer and characteristics of RuO2/TiO2/Al2O3/TiO2/RuO2 capacitors. Journal of Vacuum Science Technology A. 2017 08;35(6). 061503. Available from: https://doi.org/10.1116/1.4998425.

[53] Krusin-Elbaum L. Effect of oxygen on the electrical transport in RuO2. Thin Solid Films. 1989;169(1):17-24. Available from: https://www.sciencedirect.com/science/article/pii/S0040609089800185.

[54] Kolawa E, So FCT, Flick W, Zhao XA, Pan ETS, Nicolet MA. Reactive sputtering of RuO2 films. Thin Solid Films. 1989;173(2):217-24. Available from: https://www.sciencedirect.com/science/article/pii/0040609089901375.

[55] Magnetron Sputtering Overview; 2019. Available from: https://angstromengineering.com/tech/magnetron-sputtering/.

[56] Dietrich H. Advancing Magnetron Sputtering Technology;. Available from: https://www.thfc.de/fundamentals-of-sputtering.

[57] What is sputtering? magnetron sputtering?; 2022. Available from: https://www.semicore.com/what-is-sputtering.

[58] Leskelä M, Niinistö J, Ritala M. 4.05 - Atomic Layer Deposition. In: Comprehensive Materials Processing. Oxford: Elsevier; 2014. p. 101-23. Available from: https://www.sciencedirect.com/science/article/pii/B9780080965321004015.

[59] Johnson RW, Hultqvist A, Bent SF. A brief review of atomic layer deposition: from fundamentals to applications. Materials Today. 2014;17(5):236-46. Available from: https://www.sciencedirect.com/science/article/pii/S1369702114001436.

[60] Chu YH, Huang HH, Chen YH, Hsu CH, Tzeng PJ, Sheu SS, et al. Ultra-thin hf0.5zr0.5O2 ferroelectric tunnel junction with high current density. 2021 International Symposium on VLSI Technology, Systems and Applications (VLSI-TSA). 2021.